**BIOMIMETIC MICRO AIR VEHICLE TESTING DEVELOPMENT
AND SMALL SCALE FLAPPING-WING ANALYSIS**

THESIS

Craig E. Svanberg, Second Lieutenant, USAF

AFIT/GAE/ENY/08-M27

**DEPARTMENT OF THE AIR FORCE
AIR UNIVERSITY**

AIR FORCE INSTITUTE OF TECHNOLOGY

Wright-Patterson Air Force Base, Ohio

The views expressed in this Graduate Research Project are those of the author and do not reflect the official policy or position of the United States Air Force, Department of Defense, or the U.S. Government.

AFIT/GAE/ENY/08-M27

BIOMIMETIC MICRO AIR VEHICLE TESTING DEVELOPMENT

AND SMALL SCALE FLAPPING-WING ANALYSIS

THESIS

Presented to the Faculty

Department of Aeronautical Engineering

Graduate School of Engineering and Management

Air Force Institute of Technology

Air University

Air Education and Training Command

In Partial Fulfillment of the Requirements for the

Degree of Master of Science in Aeronautical Engineering

Craig E. Svanberg

Second Lieutenant, USAF

March 2008

AFIT/GAE/ENY/08-M27

BIOMIMETIC MICRO AIR VEHICLE TESTING DEVELOPMENT

AND SMALL SCALE FLAPPING-WING ANALYSIS

Craig E. Svanberg
Second Lieutenant, USAF

Approved:

_____//SIGNED//_____	14 March 2008
Reeder, Mark F., Civ AFIT/ENY (Chairman)	Date

_____//SIGNED//_____	14 March 2008
Cobb, Richard G., Civ AFIT/ENY (Member)	Date

_____//SIGNED//_____	14 March 2008
Huffman, Richard E., Maj AFIT/ENY, USAF (Member)	Date

Abstract

The purpose of this research was to develop testing methods capable of analyzing the performance of a miniature flapping-wing mechanism that can later be adapted to a biomimetic micro air vehicle (MAV). Three small scale flapping mechanisms capable of single plane flapping, flapping with active pitch control, and flapping/pitch with out-of-plane movement were designed using SolidWorks. The flapping-only model was fabricated on an Objet Eden 500V 3-dimensional printer.   The flapping mechanism was mounted on an aluminum plate supported by air bearings, and thrust was measured for a variety of conditions. The testing was conducted using wings composed of carbon fiber and Mylar in four different size configurations, with flapping speeds ranging from 3.5 – 15 Hertz. The thrust was measured using an axially mounted 50 gram load cell which resulted in an accuracy of $\pm$ 0.1 gram. Non-dimensional thrust and power numbers were computed. The flapping mechanism was then mounted on a 6-component force balance to measure dynamic loading, which demonstrated the ability to gather time-accurate data within a single flapping stroke at speeds as high as 15 Hz. High speed cameras operated at 1500 Hz were also used for capturing images of the structure of the wing for various testing conditions. Overall this research successfully demonstrated both qualitative and quantitative testing procedures that can be utilized in developing small scale flapping-wing micro air vehicles.

Acknowledgements

Table of Contents

List of Figures

List of Tables

BIOMIMETIC MICRO AIR VEHICLE TESTING DEVELOPMENT
AND SMALL SCALE FLAPPING-WING ANALYSIS

1. Introduction

1.1 Motivation

Technological progress in a number of areas including aerodynamics, micro-electronics, sensors, micro-electromechanical systems, and micro-manufacturing, is making it possible for the affordable development and acquisition of a new class of military systems known as micro-air vehicles (MAV). The Air Force Institute of Technology (AFIT) and the Air Force Research Laboratory (AFRL) are working together to aid in the development of the next generation of flapping-wing MAVs. According to the Defense Advanced Research Projects Agency (DARPA), a MAV is a highly maneuverable aerial robot that has a maximum dimension or 150 mm and a gross weight of 100 grams (McMichael and Francis, 1997). Larger unmanned aerial vehicles have already played an important role in military surveillance and reconnaissance operations, and the development of smaller vehicles will expand the list of possible missions that can be accomplished. Some of these future missions could include bio-chemical sensing, targeting, tracking, deployment of small payloads to remote locations, along with many others we cannot even imagine today. These missions will be possible if MAVs can fulfill their potential to attain certain attributes to include: low cost, low weight, little to no logistical "footprint," mission versatility, range, endurance, stealth, and precision (Huber, 2002).

Many of the future missions will more than likely require the ability of the MAV to remain relatively stationary, or hover, for any length of time. The two primary

1

methods for achieving hovering flight on a small scale are accomplished by either rotary or flapping wings. There is no clear cut frontrunner as to which of the two methods would better lend itself to a MAV, however, it is known for helicopters that efficiency and the ability to tolerate wind gusts diminish as scale decreases. On the other hand, one promising factor for a flapping-wing mechanism is that animals rely on the same principle to accomplish hovering flight in nature. For these reasons, there is an impetus to study flapping-wing MAVs for civilian and defense applications.

Due to the inherent small scale of a MAV, there are many technological challenges to overcome. Flapping-wing MAVs will operate at such a low Reynolds number that flowfield characteristics will be of fundamental importance. Along with aerodynamic issues, designers will have to deal with complex wing kinematics, weight and volume constraints for actuators and power supplies, high propulsive power-to-weight ratio requirements, and the ability to operate in a wide range of environments. It is clear that no man-made MAV has matched the performance and flying qualities of many small birds and insects found in nature. For this reason, it is no surprise that nature serves as an effective tool to study how a flapping-wing MAV should operate.

There are two primary methods for hovering exhibited in nature, one type can be seen with a hummingbird and the other a dragonfly. The hummingbird utilizes a method called horizontal stroke-plane hovering, which involves the wings flapping in a plane roughly parallel to the ground. A dragonfly uses inclined stroke-plane hovering, which differs from the hummingbird by having the wings beating in a plane at an angle that is inclined to the horizontal (Ellington, 1984).

The issue of what type of airflow a MAV will operate in, whether it be either turbulent or laminar, is dependent on the design and operating conditions. The transition from laminar to turbulent airflow occurs at the critical Reynolds number. This number is dependent upon various flow field and surface conditions, but generally happens at around 10,000. Many small birds fly with Reynolds numbers over 20,000 resulting in mostly turbulent airflow over their wings. For example, the hummingbird is believed to operate in a turbulent environment, with a Reynolds number based on wing chord between 5,000 and 30,000 (Snyder, Beran, Parker and Blair 2007).

1.2   Research Focus and Goals

The purpose of this research was to fabricate and test a flapping-wing mechanism in order to collect data that can eventually be used to validate computational design tools currently under development. In order to accomplish these goals, testing methods needed to be developed that were capable of measuring the extremely small fluctuating forces associated with a flapping-wing MAV.

The first step was to design and build a flapping mechanism to mimic the behavior of a biologically inspired MAV. A mechanism was designed using SolidWorks and fabricated on an Objet Eden 500V three-dimensional printing machine. Various sizes of wings were also be made to simulate different planform areas and allowed for different configurations to be tested. The first testing method used a combination of a linear air bearing table and two 0.5 Newton (50 gram) load cells. This test demonstrated the ability to measure the mean thrust generated by the flapping motion. The second type

of testing involved mounting the flapping mechanism to a six degree-of-freedom force balance to acquire time-resolved data, allowing for multiple data points to be collected within the course of a single flapping stroke. The final goal of this research was to demonstrate the potential for using photogrammetry in conjunction with high speed cameras to physically model the shape of the wing under real world conditions.

2. Literature Review

2.1   Flapping Mechanisms

The motion of wings found in nature can be quite complicated, especially for small birds capable of hovering. One of the main hurdles in designing a biomimetic flapping-wing MAV is capturing the complexity of the motion of the wing. A hummingbird wing has at least three degrees of freedom. One class of motion is the flapping stroke. This flapping stroke is the vertical motion of the wing in a plane perpendicular to ground. The second class of motion is wing rotation. This allows the wing to actively change pitch within the flapping stroke. The third class of motion involves the ability of the wing to flap in a stroke plane that is parallel to the ground. This flapping motion, when coupled with the changing pitch of the wing, is the primary mechanism allowing a hummingbird to hover. Figure 1 illustrates how these ranges of motion apply to a hummingbird.
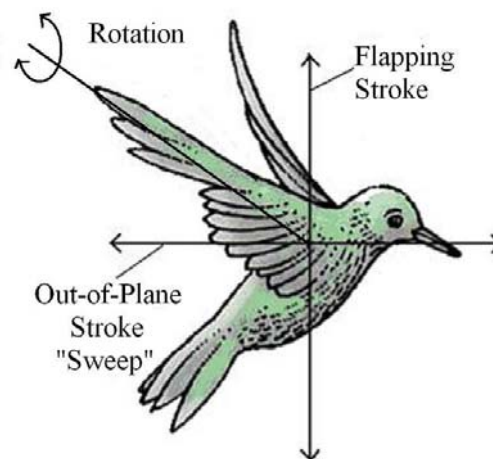
Figure 1: Hummingbird Wing Movement

One of the main goals of the overall project is to design a mechanism with a maximum of a 6" total wingspan with two wings each measuring 2.5", and a body diameter of 1". A set of secondary design goals were laid out as follows. The desired range of motion of the wings should be a flapping stroke capable of ± 80 degrees of movement, an out-of-plane stroke of ± 30 degrees and a wing rotation (pitch) of at least ± 60 degrees. The mechanism should also be capable of flapping at a frequency of 25 Hz. The ability of the wing to perform the out-of-plane stroke (sweep) of ± 30 degrees will allow the wing to perform oval and figure-eight patterns. The total target weight of the mechanism is 15 grams, and in order to analyze different wing configurations, the wings will also be removable. It is also preferred to have the actuators for the wings be variable while the mechanism is operating and not locked-in by the design.

Due to such complicated flapping patterns, functional flapping mechanisms capable of such motion prove difficult to design at small scales with the ability to lift an operational vehicle. Along with systems that operate in air, considerable work has been done with mechanisms capable of flapping a plate in water (Isaac, Colozza and Rowles, 2006). One interesting design illustrated in Figure 2, operated a single wing capable of dynamically changing pitching and flapping motions.
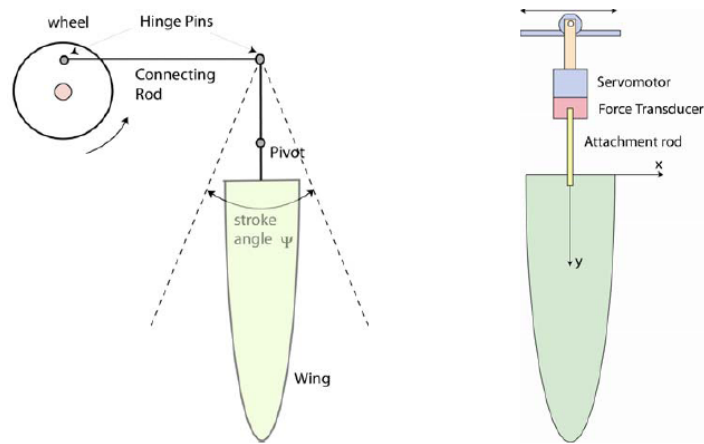
Figure 2: Flapping/Pitching Mechanism in Water (Isaac et al, 2006)

The flapping motion was driven by a connecting rod connected to a motor driven crankshaft. The connecting rod was attached to the wing through a fixed pivot joint. The pitching motion was controlled through a servomotor that was connected directly below the pivot joint. This servomotor allowed for the pitch to be independently controlled from the flapping motion, which is one of very few mechanisms capable of changing the pitch on the fly. Due to the fact that the mechanism was operated in water, the flapping frequencies were low. Designing a mechanism that can produce the higher flapping frequencies required for air and still be able to dynamically control the pitch on the fly is a considerable challenge (Gautam and Massey, 2007).

Another example design from McIntosh, Agrawal and Khan at the University of Delaware is a mechanism capable of flapping two wings while also being able to change the pitch angle. One notable feature about this mechanism was the flapping and pitching motion were controlled through the use of a single actuator. The motion created by this mechanism resembles the pitching motion created by insects, where the wing is rotated at

the top and bottom of each stroke by the use of various torsion springs and a pin follower

system. A computer model of the mechanism is shown in Figure 3.

Figure 3: Two Wing Flapping and Pitching Mechanism (McIntosh et al, 2006)

Some drawbacks to this particular mechanism are that it only operates at flapping

frequencies of 1.2 to 1.9 Hz, and the pitching profile cannot be easily changed. This

requires that the mechanism be stopped and physically reconfigured in order to produce a

different set of pitching motions.

2.2   Wing Design

Great attention must be paid to the importance of the wing structure and

articulation if a flapping-wing MAV is to be successful. These artificial wings must be

very lightweight in order to achieve high flapping frequencies, yet strong enough to

survive large oscillatory accelerations. The wings of insects are purely passive structures

which are only set into motion by triggering muscles located at the base of each wing.

These wings move with three degrees of freedom, similar to the motion exhibited by a

hummingbird (Wilson and Wereley, 2007). Due to this complicated range of motion,

designing a small scale wing with the potential to lift an operational vehicle is very difficult.

According to *The Novel Aerodynamics of Insect Flight: Applications to Micro-Air Vehicles* (Ellington, 1999), typical insect wings twist 10 to 20 degrees along the length of the wing with the angle of attack at the wing base higher than at the wing tip. This twisting of the wing is achieved through inertial-elastic effects which result in a wing camber in the chordwise direction where the camber shape is ultimately dictated by the arrangement of the wing veins (Ennos, 1988). This change in the overall shape of the wing is dominantly characterized by inertial forces, where aerodynamic loads contribute very little (Combes, 2003). Insects must also be able to rotate their wings during stroke reversal in order to orient them with the proper angle of attack with respect to the oncoming flow. This fast rotation is necessary to utilize the unsteady flow mechanisms which are considerable in lift generation for insects (Dudley and Ellington, 1990).

Although many researchers have noted the importance that flexible wings play in the aerodynamics of flapping flight, there are relatively few studies dealing with flexible rather than rigid wings in flapping flight (Ho, 2003). Much of the numerical and experimental work so far has centered around rigid wings because the aeroelastic interaction between the wing and surrounding fluid could then be neglected, which greatly reduces the overall complexity of the problem. Research conducted by Shyy compared the lift to drag (L/D) ratio of three separate airfoils of the same camber but with different membrane flexibilities (Shyy, 1997). When compared to the rigid wing, the highly flexible latex membrane wing exhibited better L/D performance at higher angles of attack but worse L/D ratios at lower freestream velocities resulting from the

decreased pressure differential between the upper and lower membrane surface. A hybrid wing exhibited equal to or greater performance compared to the highly flexible wing at all angles of attack and was not as sensitive to L/D drop at lower freestream velocities. From this testing, they concluded that modulating the flexibility of the wing could improve the aeroelastic characteristics and ultimately the flight performance.

Ho et al, compared the coefficient of thrust (C_T) for two equally sized wings made with the same sized carbon fiber spars to analyze the role that stiffness distribution plays in thrust production (Ho, 2003). The coefficient of thrust for forward flight is defined as:

$$C_T = \frac{T}{\frac{1}{2}\rho U^2 S} \qquad (1)$$

where

T = thrust force

ρ = local air density

U = forward flight velocity

S = wing planform area

One of the wings used a paper membrane while the other was a Mylar membrane. The paper membrane was less flexible than the Mylar membrane due to the higher stiffness of the paper. The result from the testing of the two wings is shown in Figure 4.
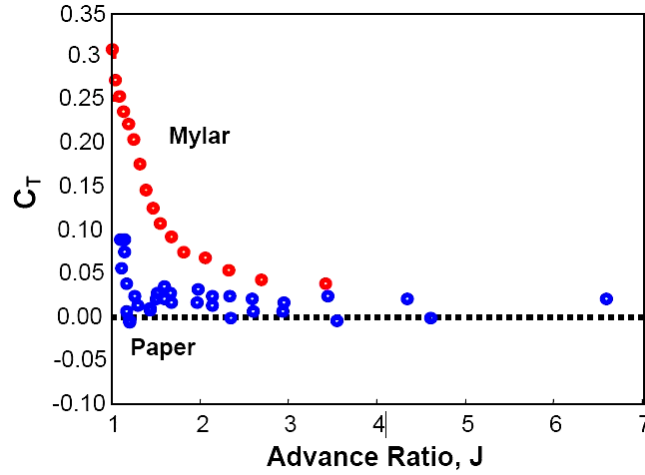
Figure 4: Wing Stiffness Effect on Thrust Production (Ho et al, 2003)

The coefficient of thrust for both wings was taken for varying advance ratios (J). The method for calculating the advance ratio is defined in Equation 2.

$$J = \frac{U}{2\Phi fb}$$

(2)

where

U = forward flight speed

Φ = total flapping angle

f = flapping speed

b = wing span

Ho et al, notes that the breakpoint between quasi-steady and unsteady flow happens when J = 1, with J > 1 considered quasi-steady and J < 1 corresponding to unsteady flow regimes (Ho, 2003). As seen in Figure 4, the thrust performance differs greatly and it diverges faster as the advance ratio decreases. Ho observed that over a

large number of different wing designs tested that stiffer membrane wings did not produce thrust, while more flexible membranes did (Ho, 2003). This testing demonstrated the effect that wing stiffness had on the ability of their specific wing design to increase thrust.

Wilson and Wereley, part of a research group from the University of Maryland, designed and constructed flexible membrane wings to analyze passive deformations with varying spar configurations and torsional rigidity (Wilson and Wereley, 2007). The team used a simplified aerodynamic analysis of insect hovering given by Ellington for modeling the lift capacity of a MAV, given in Equation 3 (Ellington, 1999).

$$m = 0.387 \left(\frac{\Phi^2 n^2 R^4 C_l}{AR} \right) \tag{3}$$

where

m = mass of vehicle (kg)

Φ = flapping angle (radians)

n = flapping frequency (Hz)

C_l = lift coefficient of wing

AR = aspect ratio

R = wing span / 2 (m)

This equation was primarily used to solve for the main design parameters of the model and to find the length of the wings used in the study. The finished wings can be seen in Figure 5, along with their dimensions.
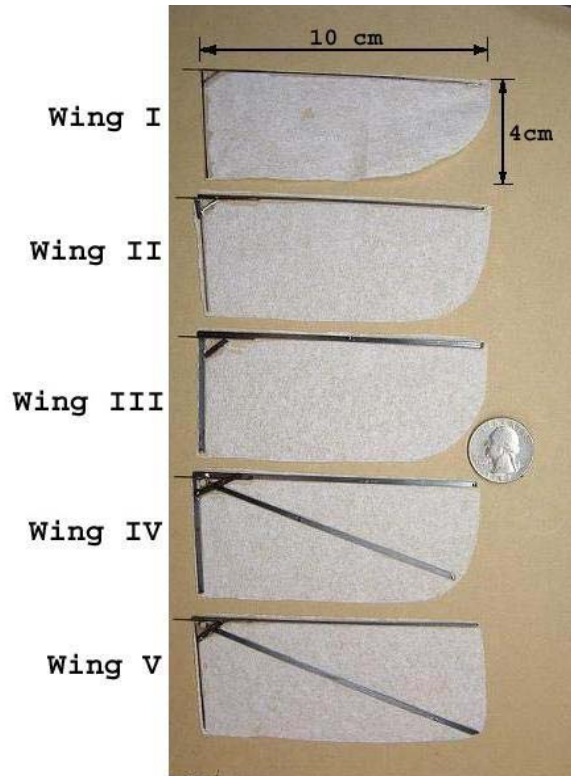
Figure 5: Carbon Spar Wings (Wilson and Wereley et al, 2007)

The wings were constructed using carbon fiber rods for spars and tissue paper as a thin membrane secured to the spar frame with epoxy. The spanwise structural stiffness varied for each wing resulting in unique wing deformations for each configuration. Due to the diagonal spar extending through the center of the wing, the fourth and fifth configurations proved to have the highest performance in terms of thrust production (Wilson and Wereley, 2003). The cross spar increased the amount of thrust generated by increasing the moment of inertia about the leading edge. This increased inertia resulted in larger tip twists at stroke reversal, pitching the outer sections of the wing to lower angles of attack with less of a bluff body orientation (Wilson and Wereley, 2003).

Another design using a similar wing layout is the remote control dragonfly manufactured by FlyTech, seen in Figure 6.
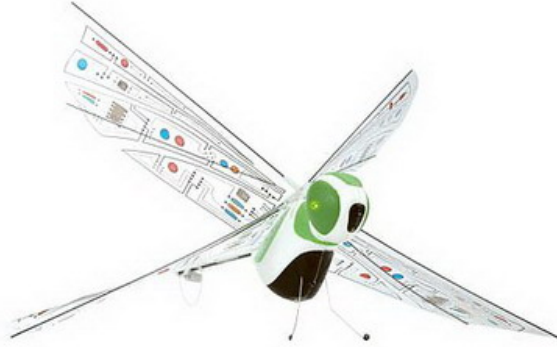
Figure 6: FlyTech R/C Dragonfly

The R/C Dragonfly has a rigid leading edge with a single diagonal spar, and a flexible plastic membrane. The wing length from root to tip is 8 inches with a chord length of 3.5 inches. These wings are physically too long to be considered for a flapping wing MAV, however, this particular configuration serves as a useful model for wing construction.

2.3   Force Measurement

In order to measure the forces produced by a flapping mechanism, load cells and force balances are commonly used for these types of measurements. Load cells and force balances are typically made using either single or sometimes multiple strain gauges. A strain gauge is a series of thin wire filaments wound in a serpentine fashion and placed in a Wheatstone Bridge configuration like that seen in Figure 7 below.
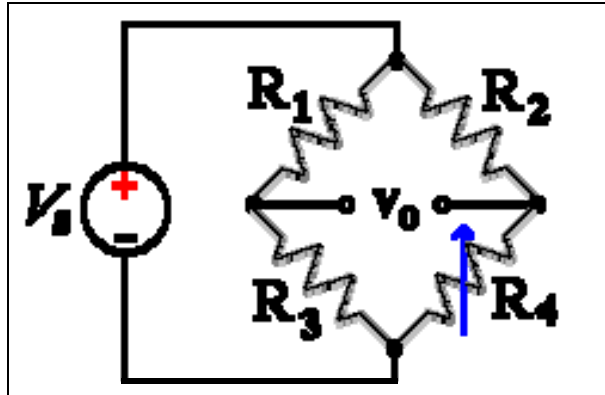
Figure 7: Strain Gauge/Wheatstone Bridge Configuration

Voltage is supplied to the strain gauge and as a load is applied to the wire

filaments, they will either elongate or shrink, changing the resistance in the wires

(Gamble, 2006). This variation in resistance results in different input and output voltages

from the strain gauge. The difference in voltage is then used to calculate the strain.

Using Hooke's Law for a linear relation, the stress in a material can be deduced by

multiplying the strain with the material's modulus of elasticity. Lastly, the forces

associated with the initial deformation of the strain gauge can be calculated by

multiplying the stress by the wire's cross-sectional area. A design for a force balance by

Jadhav Gautam and Kevin Massey from the Georgia Institute of Technology was used to

measure the lift and thrust of their flapping mechanism, which can be seen in Figure 8.
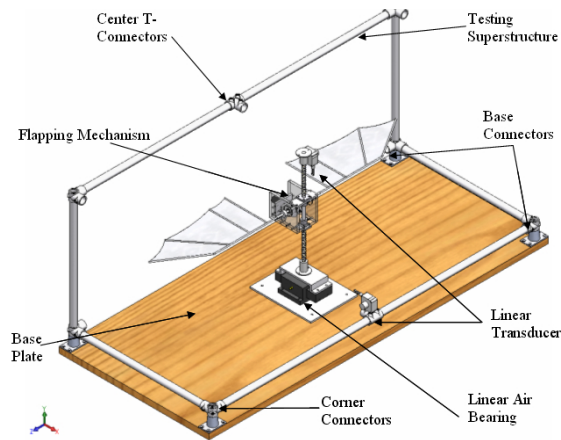
Figure 8: 2-Component Force Balance Design (Gautam and Massey et al, 2007)

This force balance suspended the model from a force transducer for measuring lift in the Y direction, and was mounted onto a linear air bearing with another transducer measuring the thrust force. Another method for measuring the forces of a flapping wing mechanism involved strain gauges, used by Wilson and Wereley from University of Maryland. The arrangement of how the strain gauge was mounted is shown in Figure 9.
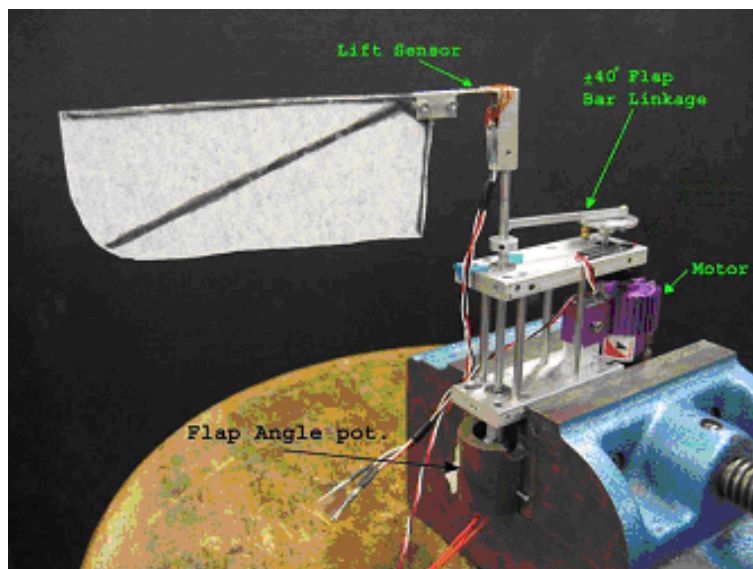
Figure 9: Strain Gauge Load Measurement (Wilson and Wereley et al, 2007)

The wing mount has a thin flexure to which the load sensor was attached. The vertical lift generated by the wing is directed vertically, perpendicular to the stroke plane of the wing and creates a bending moment at the flexure which is measured by the load cell. The lift force is averaged over several complete flap cycles due to electrical noise and mechanical vibrations.

2.4   Photogrammetry

It is also important to be able to understand the reasons for loading on MAVs. Measurements of wing deformation throughout the flapping cycle are beneficial for understanding these loads. Photogrammetry is a method for calculating the three dimensional coordinates of an object by using two or more cameras, and is a useful tool for determining and measuring movement or deflection of a test object. One early application of this type of technology was called topographic photogrammetry and was used for creating aerial surveys and maps. Modern photogrammetry typically uses digital cameras along with computer analysis software to measure hundreds, or sometimes thousands, of target points that are located on the test object.

Photogrammetry uses multiple images of a target to triangulate and compute an objects position in 3D space. A photogrammetry system must be calibrated in order to produce useful data. For calibration of a photogrammetry system, it is necessary to identify some basic parameters of the cameras. Typical photogrammetry software is capable of computing the internal camera parameters by analyzing photos of a known target grid, provided with the computer software. One example of this type of target grid

can be seen in Figure 10, which consists of black and white triangles with a coded pattern of dots in each corner.
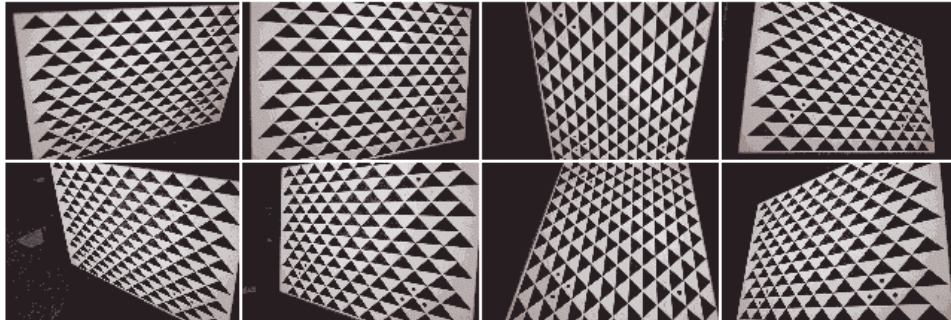

Figure 10: Photogrammetry Calibration Target Grid (Eos Systems Incorporated et al, 2007)

One popular software program for photogrammetry is called PhotoModeler Pro, which uses the grid in the above figure for camera calibration. The calibration procedure requires that the camera take multiple images of the calibration grid from all four sides, then the software can automatically process the photographs to determine the necessary parameters of the camera. For clear images that result in the greatest accuracy, it is best to have a high contrast ratio with either light or dark colored targets on a background of opposite color. Even though it is more common to use a light colored target with a dark background, a clear wing material would necessitate the use of dark markers. These markers would also have to be extremely lightweight so they will not change the properties of the wing material.

The procedure for arranging a photogrammetric system also requires some planning as to the number and distribution of the cameras, also called the photogrammetric geometry. A general guideline is to place the cameras at convergent

viewing angles when focused on the target, in both the vertical and horizontal planes if possible, with an angular separation of about 70-90 degrees. When adjusting the cameras to get the target object in focus it is generally best to set the aperture to a low setting. Having a smaller aperture results in greater depth of field, which allows for a larger portion of the object to be in focus. When using a small aperture setting, it also means that less light will be entering the lens requiring either brighter illumination of the target or slowing down the shutter speed. It is usually a good idea to have cameras with a shutter speed of more than 30 milliseconds to be placed on a tripod to avoid movement of the camera which can cause streaking of the image.

Overall, the accuracy of the entire photogrammetry system depends on the number and resolution of photographs, the angles between the photographs, the number of reference points and the quality of the cameras being used. The accuracy corresponds to the fraction of the overall size of the target object the software can accurately compute. According to information provided by the photogrammetry software program called PhotoModeler, the typical accuracy ranges from 1 in 200 for low resolution cameras (pixel resolution less than 512 x 512) to about 1 in 8000 for high resolution cameras (pixel resolution greater than 2000 x 2000). To put this in perspective, for a six foot object, the measurement accuracy will be about a third of an inch with a low resolution camera and within one hundredth of an inch for a high resolution camera.

Kelly Stewart and Roberto Albertani from the University of Florida use a process similar to photogrammetry called visual image correlation to study flexible wing elastic deformation (Stewart and Albertani, 2007). Visual Image Correlation (VIC) provides a means of measuring in-plane and out-of-plane displacements for a test specimen

undergoing any combination of motion and deformation. As with photogrammetry, VIC uses multiple cameras to triangulate target points on the surface of a test specimen. The VIC software then tracks the movement of every target throughout each frame, providing the motion and deformation of the specimen. The experimental setup for the VIC camera system is shown in Figure 11.
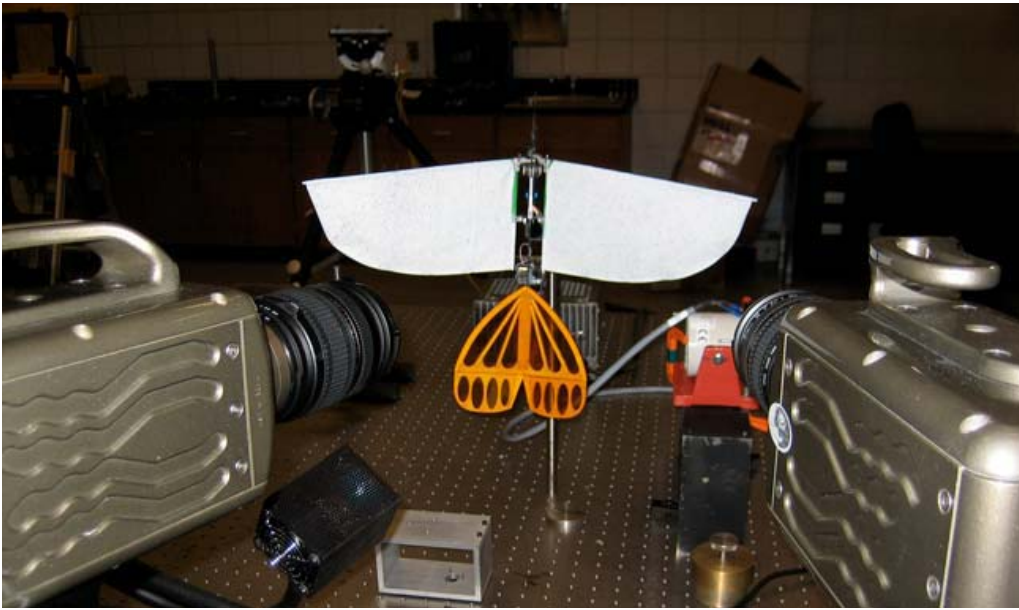
Figure 11: Visual Image Correlation Camera System (Stewart et al, 2007)

The testing was conducted with rigid and flexible wings connected to an electromagnetic shaker with a frequency of 5 and 10 Hz. The cameras were set to record at 100 frames per second with 1 second of data used for post processing. The position data gathered from these tests was successfully used for decoupling the kinematics of wing motion from the deformation of a flapping wing (Stewart and Albertani, 2007).

3. Methodology

3.1 Experimental Apparatus and Setup

3.1.1 *Flapping Mechanism*

The first step in this project was to develop a viable flapping wing mechanism that can be used to verify testing methods. It was decided to build a mechanism where the wings were actuated by rods connected to a rotating crankshaft. Due to the extremely small scale of the original design constraints set forth by AFRL, a slightly larger scale mechanism seemed prudent for this stage of the research for manufacturing purposes. Before the actual mechanism could be designed and built, a proof-of-concept model was drawn using SolidWorks. The first phase of the model design led to a flapping motion achieved through the motion of a crankshaft. This flapping only model is shown in Figure 12.
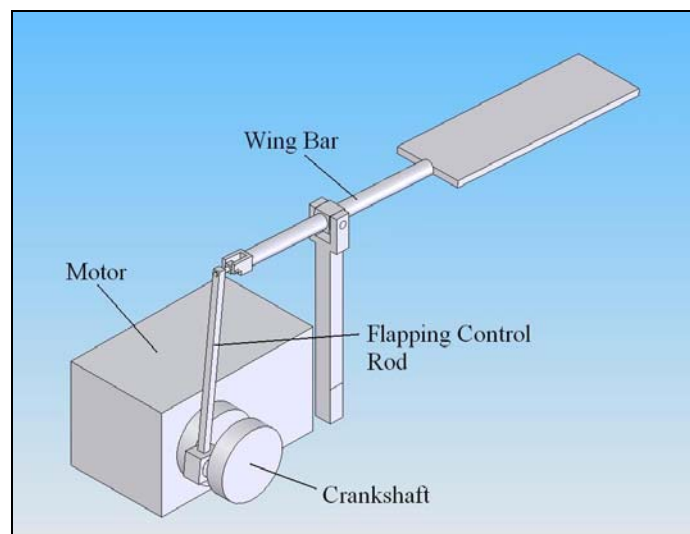

Figure 12: SolidWorks Flapping Only Model

This flapping model also allowed for different ranges of motion to be examined by changing the diameter of the crankshaft and moving the pivot point on the wing bar, resulting in larger flapping angles. The second and slightly more complicated stage of the SolidWorks model was determining if it would be possible to change the pitch of the wing with the same crankshaft. In order to achieve this motion, an additional node was added to the end of the crankshaft that was slightly out of phase from the flapping node. This pitching node on the crankshaft was then connected to the wing bar by a rod that attached to a pivot point extending perpendicular from the end of the wing bar, seen in Figure 13.
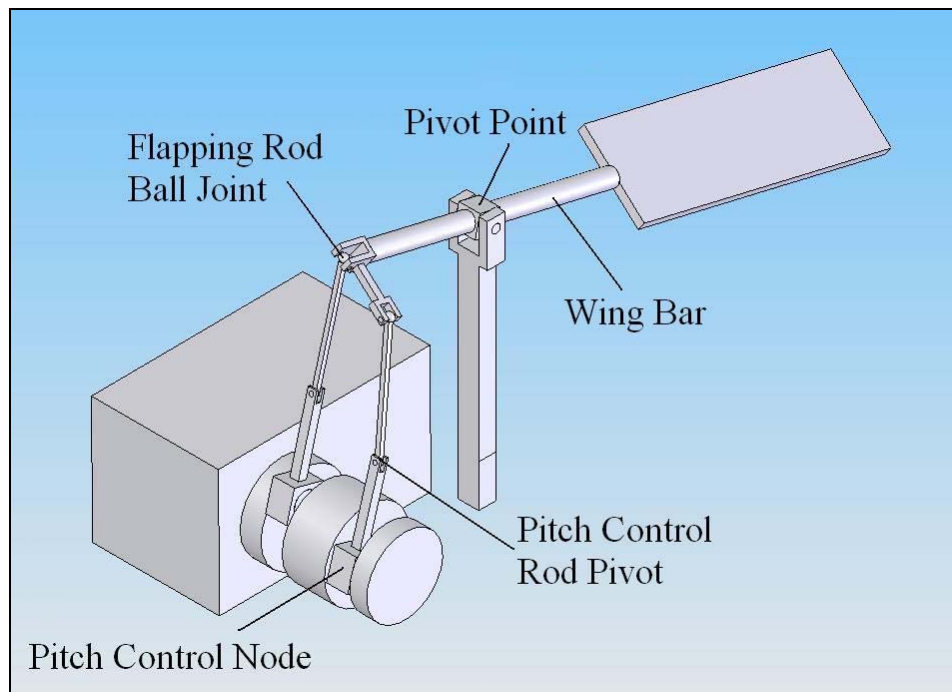

Figure 13: SolidWorks Flapping-Pitch Model

The addition of the pitch control also meant that the rod connecting the pitching node on the crankshaft to the wing bar was no longer moving in a single plane at the

attachment point. In order to account for this, the pitch control connecting rod had an additional pivot point halfway up the rod that allowed it to move out-of-plane throughout the flapping stroke. Another attachment point that needed to be altered to allow for pitch variation is the pivot point on the wing bar. This pivot point had to be modified in order to allow the bar to rotate axially while still being able to flap in a single plane. The attachment point of the flapping control rod to the wing bar was also changed to a ball joint to give it the necessary range of motion.

The final movement to demonstrate with the SolidWorks model was the out-of-plane flapping motion. This particular movement allowed for the wing to sweep back and forth in a plane perpendicular to the vertical flapping stroke. As with the pitch control, an additional node was added to the end of the crankshaft that would control the out-of-plane motion. It was determined that one of the easiest ways to accomplish this motion was to rotate the arm that held the pivot for the wing bar. This allowed for the joint at wing bar pivot point to remain the same without adding the complexity of another degree of freedom. The final design operational design is illustrated in Figure 14.
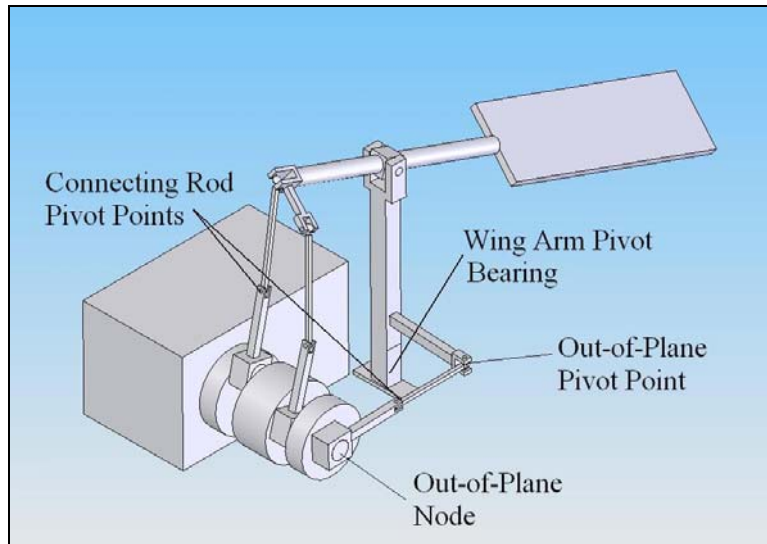
Figure 14: SolidWorks Flapping, Pitching and Out-of-Plane Model

With the addition of the out-of-plane motion, this meant that none of the connecting rods would be traveling in a single plane and needed an extra pivot point. An illustration of the model while in motion can be seen in Figure 15.
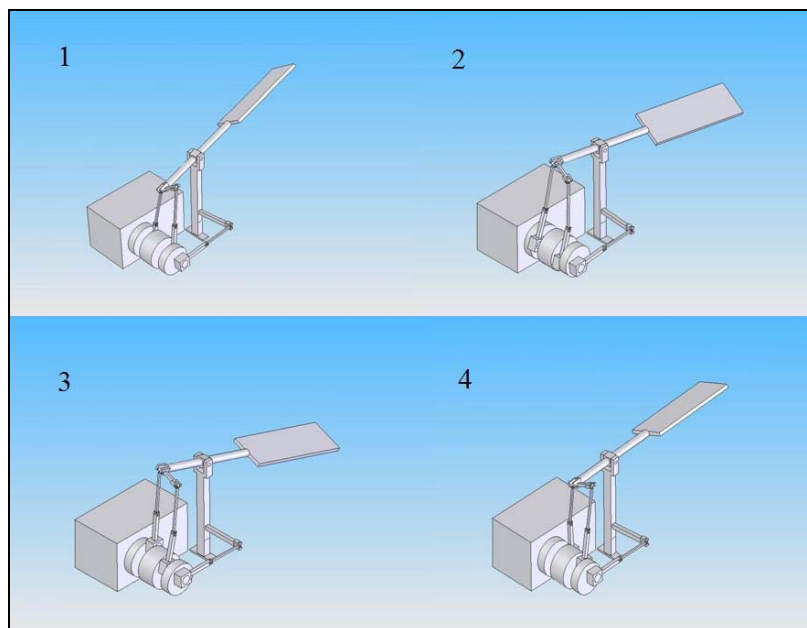
Figure 15: Flapping Model in Motion

The motion of the three degree-of-freedom model could also be calculated within SolidWorks. An illustration of how the reference points were positioned on the wing, along with a graph showing their location throughout a single cycle can be seen in Figure 16.
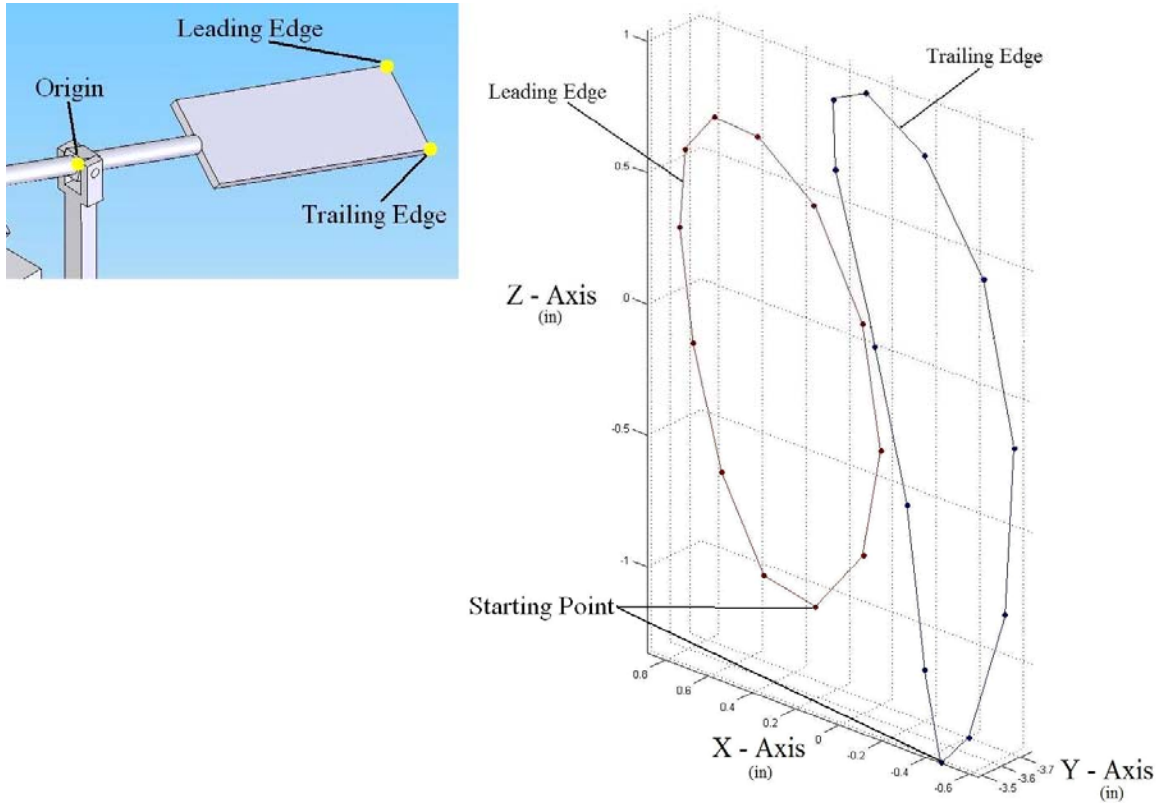
Figure 16: 3-D Wing Position Tracking

After determining the position of the wing with respect to the origin (wing pivot point), the flapping, sweep and pitch angles were also be calculated. Table 1 shows these three angles along with the X, Y and Z coordinates of the leading and trailing edges of the wing.

Table 1: SolidWorks 3-D Wing Position and Flapping, Sweep and Pitch Angles

Cycle	Leading Edge Position			Trailing Edge Position			Flapping Angle (deg)	Sweep Angle (deg)	Pitch Angle (deg)
	X	Z	Y	X	Z	Y			
1/12	0.23	1	-3.62	-0.47	1.33	-3.48	-18.15	-1.84	24.69
2/12	0.07	0.78	-3.68	-0.57	1.21	-3.51	-15.43	-3.83	32.98
3/12	0.04	0.39	-3.74	-0.64	0.77	-3.62	-8.92	-4.60	28.75
4/12	0.14	-0.06	-3.76	-0.61	0.16	-3.7	-0.77	-3.60	16.17
5/12	0.32	-0.46	-3.72	-0.47	-0.43	-3.7	6.83	-1.15	2.18
6/12	0.52	-0.69	-3.65	-0.25	-0.86	-3.64	11.96	2.07	-12.43
7/12	0.7	-0.72	-3.62	-0.02	-1.04	-3.6	13.61	5.22	-23.90
8/12	0.83	-0.56	-3.62	0.15	-0.96	-3.62	11.72	7.53	-30.42
9/12	0.88	-0.23	-3.65	0.21	-0.64	-3.7	6.68	8.38	-31.26
10/12	0.83	0.2	-3.66	0.11	-0.1	-3.76	-0.77	7.22	-22.32
11/12	0.68	0.64	-3.64	-0.1	0.54	-3.72	-9.08	4.45	-7.27
12/12	0.46	0.95	-3.61	-0.31	1.09	-3.58	-15.83	1.15	10.21

The X-axis refers to the chordwise direction, the Z-axis is the vertical direction and the Y-axis is the spanwise direction. The X, Y and Z positions of the leading and trailing edges were taken with respect to the origin, which was also the pivot point of the wing. The flapping and sweep angles were calculated with respect to the mid-chord line. Although this SolidWorks proof-of-concept model did not satisfy the required ranges of motion set forth in Chapter 2, it was a useful tool to illustrate how all three motions can be accomplished with a single crankshaft.

After it was demonstrated that the necessary movements can be accomplished with a single crankshaft driven design, a mechanism used for actual testing was built. As was the case with the verification models, the first mechanism would be a flapping only design. The fact that it would be a flapping only mechanism with no method for actively varying pitch also meant that it would have to test flexible wings with a passive pitch in order to produce thrust. Since the mechanism was fabricated using 3-D printing material,

it was desired that any moving parts be isolated with miniature ball bearings for added durability and to avoid plastic-on-plastic contact wherever possible. In order to get the desired movements from various attachments and pivot point throughout the mechanism, parts manufactured for micro scale remote control airplanes were also purchased.

To start the design process, a drive mechanism had to be determined. It was decided to go with a single motor that would drive two counter rotating crankshafts which would be connected by a system of gears. The gears chosen that would attach to the crankshaft were made from nylon with a metal pinion gear attached to the motor. The crankshafts themselves had two different attachment points for the flapping control connecting rod at different distances from the center. The two separate radial distances allowed for adjustment of the total throw of the connecting rod which ultimately controls the flapping angle of the wing. The crankshaft with dimensions in inches can be seen in Figure 17.
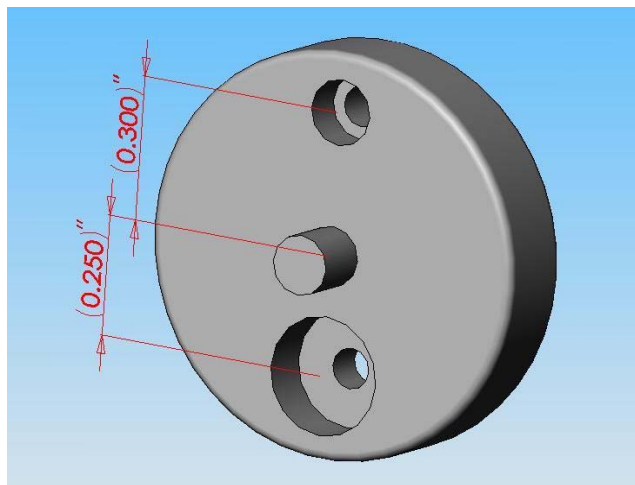

Figure 17: Flapping Mechanism Crankshaft

Each individual crankshaft consisted of two individual pieces connected by a Du-Bro 2-56 swivel ball link manufactured for model planes. This part provided the desired ranges of motion and was durable enough to withstand the flapping frequencies of the mechanism, which ranged from 3.5 to 15 Hz for the first phase of this project. The crankshafts themselves were held in place on one end by the main body of the flapping mechanism, and by a support arm on the other end. Since the crankshaft is also the main moving part of the mechanism, they were held in place by ball bearings at both attachment points.

The lower support arms that secure the open end of the crankshaft were designed to come from underneath so they would not interfere with the rotation of the crankshaft. The support arms were also secured on the underside of the main body using screws. The upper support arms were also attached to the main body and used as an attachment point for the flapping arm. In order to achieve the single degree-of-freedom necessary to flap in a single plane only, ball bearings were also used for the pivot point of the flapping arm to minimize the amount of free play in the joint. The lower and upper support arms can be seen in Figure 18.
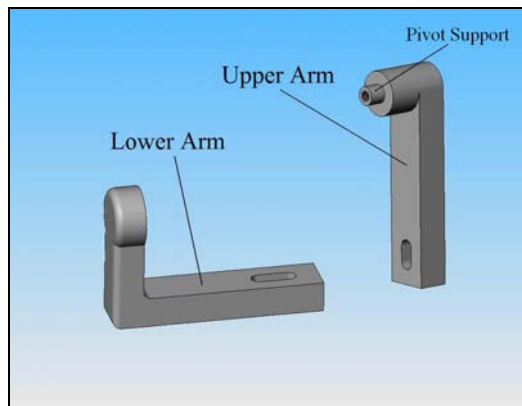

Figure 18: Flapping Mechanism Lower and Upper Support Arms

The most intricate part of the entire mechanism is the pivot arm for the wing.

This part had to attach to the flapping control rod and also be capable of pivoting on the

upper support arm. In order to attach to the flapping control rod, each pivot arm had

multiple mounting points to place a Du-Bro micro ball link. As with the two separate

mounting holes on the crankshaft, the holes on the pivot arms allowed for adjusting the

flapping motion of the wing as well. The micro ball links are essentially miniaturized

ball joints that were perfect for this kind of joint without having to design a part suitable

for this application. The pivot arm was then attached to the upper pivot arm with a fine

thread metal screw and supported around ball bearing. The portion of the pivot arm that

held the wing had a small set screw that can be tightened to keep the wing securely

attached and free from rotating, while also allowing them to be removed. A motor mount

was also designed to hold the small electric motor in place above the crankshaft, which

could be adjusted to allow the drive gears mesh properly. Figure 19 shows the pivot arms

and motor mount.
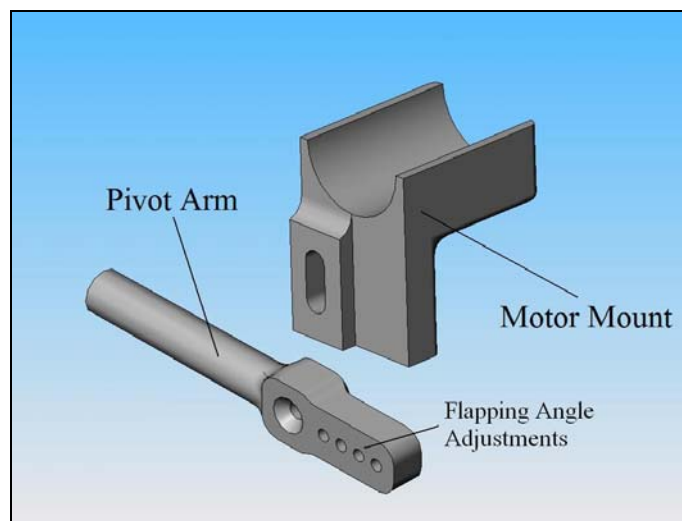
Figure 19: Flapping Mechanism Pivot Arms and Motor Mount

The final piece that needed to be designed was the main body. This part served as the mounting point for all the support arms, crankshafts and motor mount. The crankshafts were held in place by ball bearings that were press fit into the main body to hold them securely and free from rotating. The support arms and motor mount were all held in place by standard 4-40 screws with mounting holes created in SolidWorks. The main body of the flapping mechanism can be seen in Figure 20.
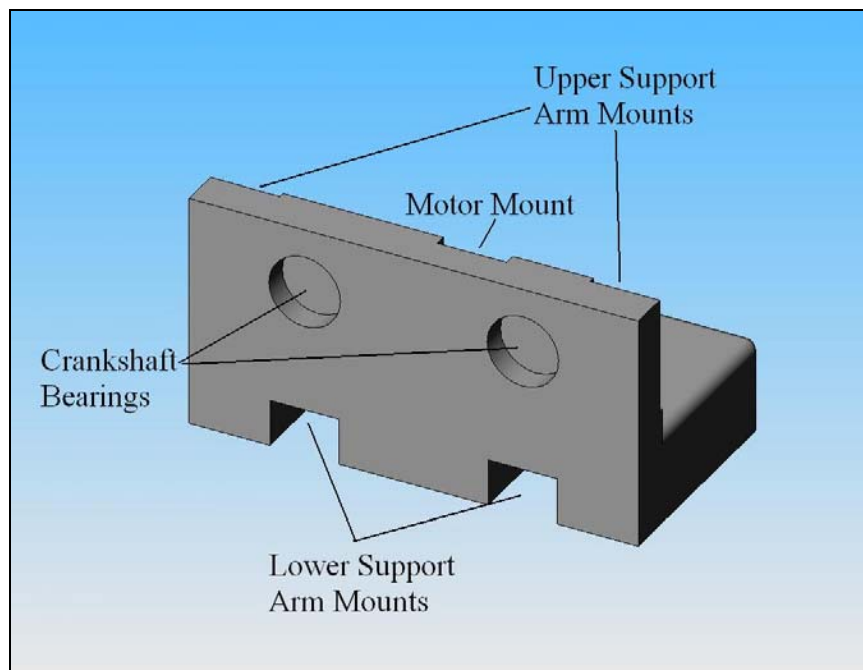

Figure 20: Flapping Mechanism Main Body

All of the parts were then test fit in SolidWorks to verify proper alignment, and the completed model is shown in Figure 21. The model was also animated to check for any interference between the moving and stationary parts.
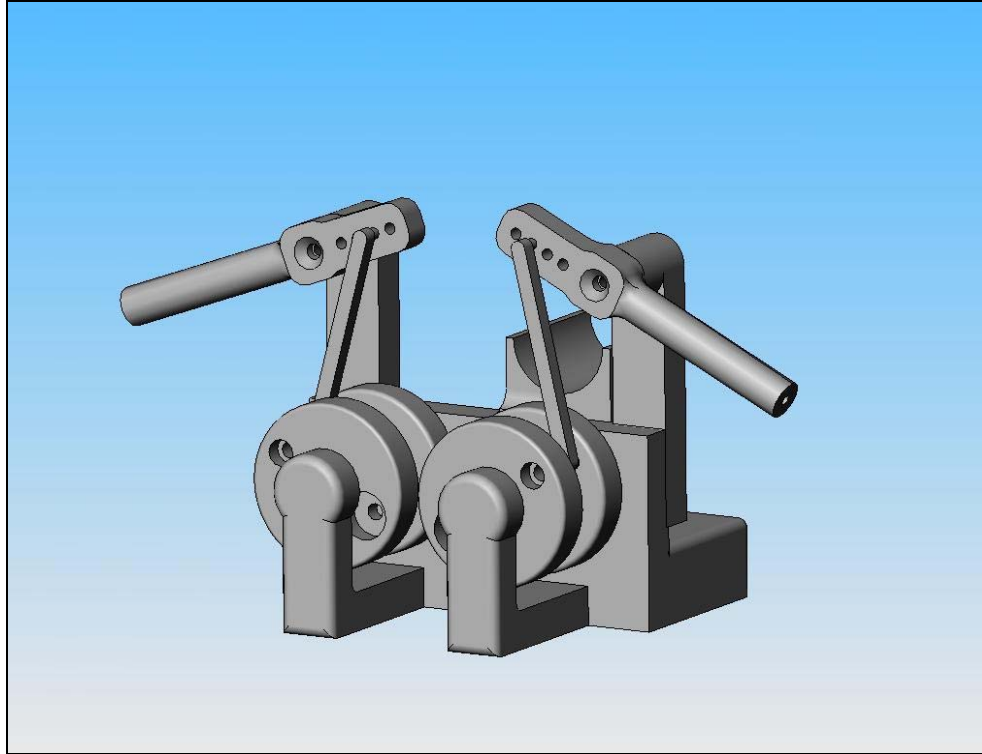
Figure 21: Completed SolidWorks Model of Flapping Only Mechanism

After all of the parts for the flapping-only mechanism were designed and test fit in SolidWorks, they were fabricated using an Objet 3-dimensional printer. The structural material used in the printer was Verablue Fullcure 840. The rods that connected the crankshaft to the pivot arm were made from the Du-Bro micro ball links and 2-56 swivel ball links, which can be seen in Figure 22. The two separate pieces were press fit together, and the threaded coupler allowed for adjustment to the total length of the connecting rod. This proved to be very useful in adjusting the pivot arm location so that it would rotate the same amount above and below horizontal.
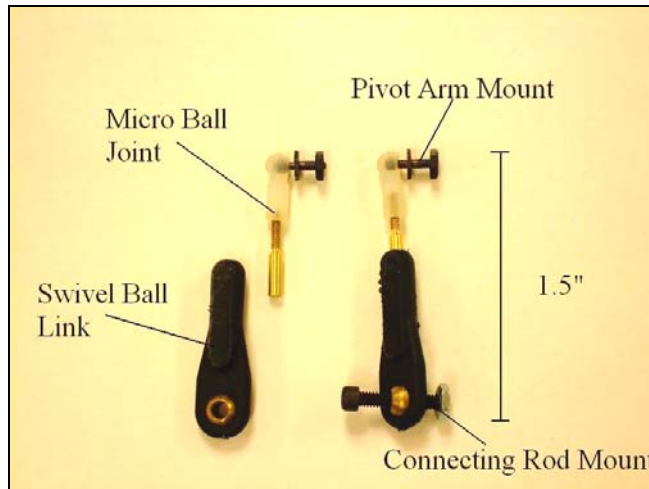
Figure 22: Flapping Mechanism Connecting Rod

The 2-56 socket head cap screw provided with the Du-Bro ball links also served as the hardware that physically held the two-halves of each crankshaft together. The ball and socket joint attached to the pivot arm and was secured using Loctite thread locker to prevent the nut from becoming loose and backing off. The nylon gear used to turn the crankshaft was then centered and glued in place using epoxy. The completed crankshaft is shown in Figure 23.

Figure 23: Completed Crankshaft

The electric motor used to power the flapping mechanism was a Faulhaber DC motor with a 7 tooth pinion gear. With 48 tooth gears used for the crankshafts, the final drive ratio was 6.85:1. Since the placement of each crankshaft with respect to one another could not be changed, only 48 tooth gears would work for this particular configuration. However, since the motor mount can be raised and lowered, different sized pinion gears could have been used to change the final drive ratio if it were necessary. The completed flapping mechanism can be seen in Figure 24, along with the final dimensions.
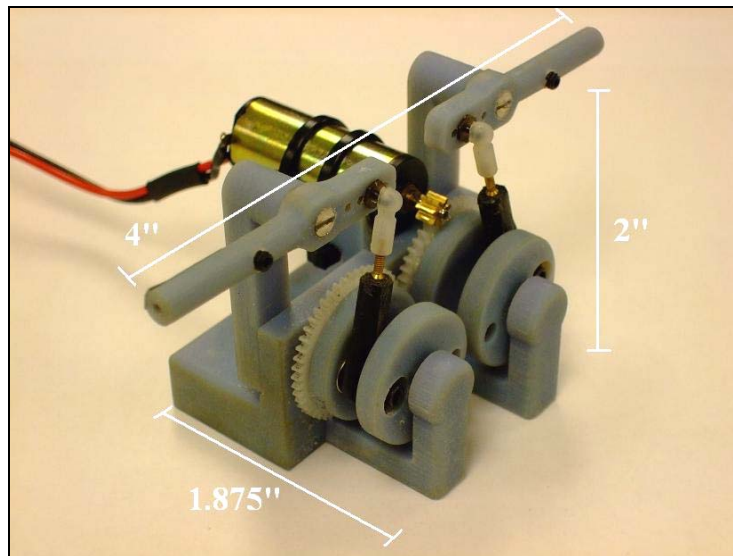
Figure 24: Completed Flapping Only Mechanism

The total flapping mechanism weighs 67 grams (0.147 pounds), including the motor weight of 23 grams. The underside of the main body had four threaded holes used to mount the model. The first of two mounts was constructed out of 1/4 inch steel plate and attached to a telescoping rod fixture. The second mount was used to attach the

33

mechanism to the six degree-of-freedom force balance. Both of the mounts can be seen in Figure 25.

Figure 25: Flapping Mechanism Mounting Fixtures

The mount used for the force balance slid over the end of the balance and was held in place using three Allen screws. In addition to the flapping-only mechanism designed in SolidWorks and built using the 3-D printer, a second model capable of actively changing the pitch of the wing throughout the flapping stoke was also designed. As with the proof-of-concept models discussed earlier in this section, the flapping-pitch model used a pair of counter-rotating crankshafts to produce the flapping and pitching motion of the wings. Figure 26 shows the flapping-pitch model fully assembled in SolidWorks.
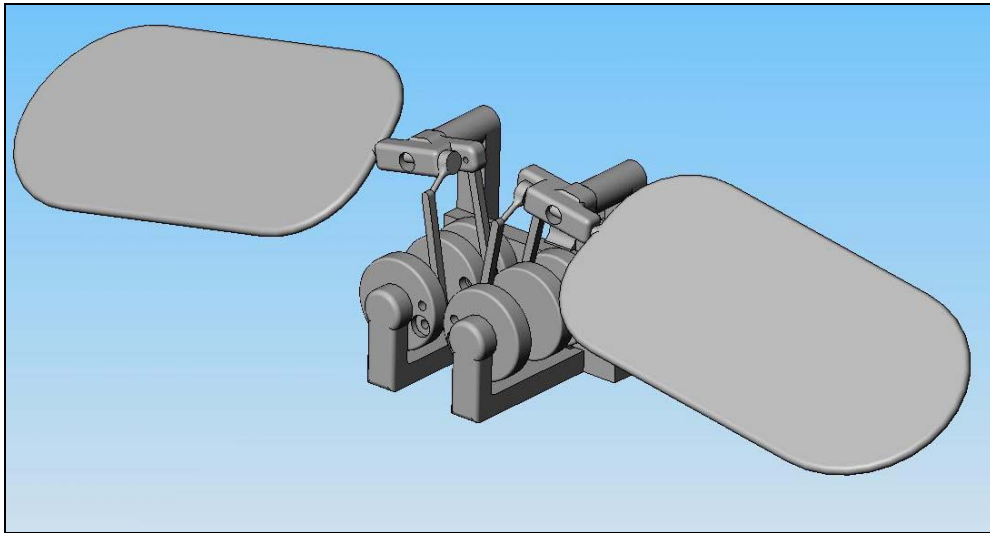
Figure 26: Flapping – Pitch Combination SolidWorks Model

The physical dimensions of this model are the same as the flapping only mechanism, using many of the same parts. Each crankshaft has two separate nodes that are 25 degrees out-of-phase from one another, resulting in the connecting rods being at separate vertical positions as the crankshafts rotate. This difference in position of the connecting rods controlling the flapping and pitching movements of the mechanism allow for the pitch of the wings to change. An illustration of the model in motion at various points can be seen in Figure 27.
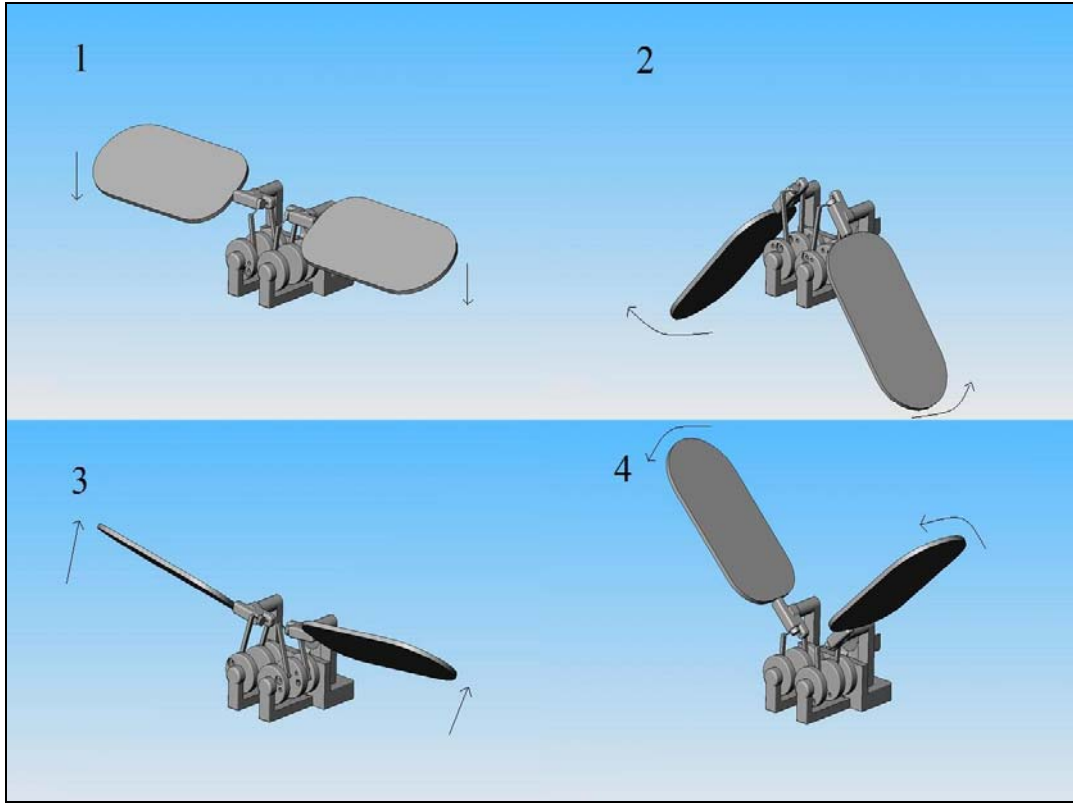
Figure 27: Flapping-Pitch Model in Motion

As was the case with the flapping only model, the most complex part of the flapping-pitch model is the pivot point connecting the wing to the rest of the mechanism. This pivot joint allows for only two degrees of freedom, one being the vertical flapping motion of the wing and the other the axial rotation of the wing varying the pitch. A magnified view of this pivot arm can be seen in Figure 28.
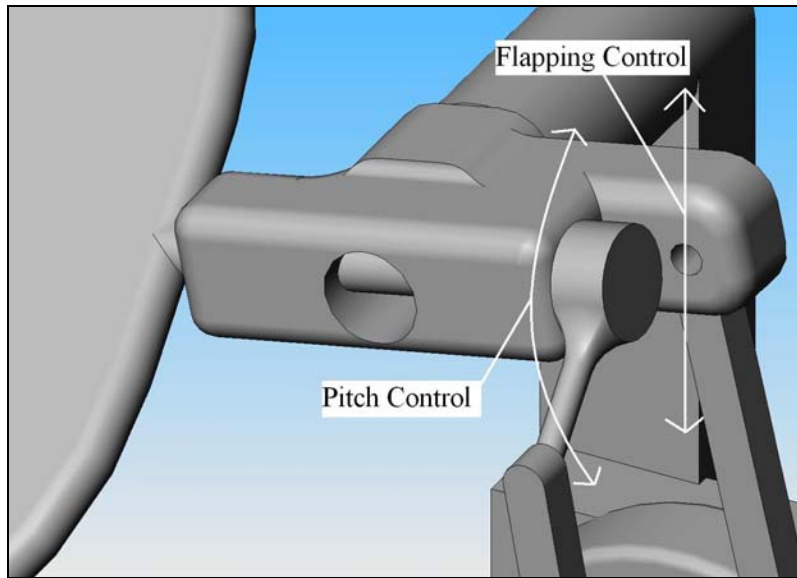
Figure 28: Flapping–Pitch Model Pivot Joint

After attempting to fabricate, this particular pivot configuration proved difficult to replicate on a physical model due to wear of the Objet printing material from the motion of the wing rotating within the pivot. A stronger type of material must be used to fabricate this pivot joint to minimize wear and free-play between the two parts. A connection system would also have to be designed to allow the wings to be removed from the mechanism. Once these two issues are overcome, this mechanism would serve as a candidate system for testing rigid and flexible wings with active pitch control. As for this research, all of the testing was conducted using the flapping-only mechanism.

3.1.2 Wing Construction

The flapping wings used in this research were very similar to those designed by Wilson and Wereley from the University of Maryland, and the R/C Dragonfly discussed in Chapter 2. These wings have the same basic design principles with an aspect ratio of

2, commonly exhibited by insects. The wings constructed for this experiment can be seen in Figure 29.

Figure 29: Flapping Wings Used For Testing

These wings were constructed using carbon fiber rods for spars and structural support, and Mylar was used for as the flexible membrane material. The Mylar is attached to the carbon fiber rods using thin layers of lightweight adhesive tape, which had a negligible impact on the inertial and aeroelastic properties of the primary materials. The weight and dimensions of the four wing configurations can be seen in Table 2.

Table 2: Wing Properties

Wing	Weight (g)	Spar Length	Chord Length	Wing Span
1	0.89	4"	2"	12.1"
2	0.79	3.5"	1.75"	11.1"
3	0.73	3"	1.5"	10.1"
4	0.59	2.5"	1.25"	9.1"

The wing spar was the thickest piece of carbon fiber rod used with a diameter of 0.05" for added stiffness. A slightly smaller rod with a diameter of 0.04" was used for the root chord and diagonal spar pieces. This smaller diameter allowed for more aeroelastic deformation allowing the wing to be more flexible under flapping conditions. The shorter rod that defines the root chord of the wing is attached to the main spar using a part designed in SolidWorks called the wing root brace, seen in Figure 30. This part holds the two pieces together at a 90 degree angle and prevents them from rotating around the axis of the main spar.
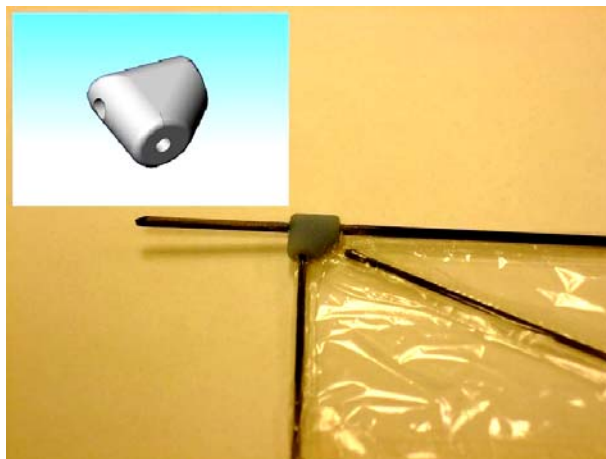
Figure 30: Wing Root Brace

In order to construct the wings, first the planform of the wing was printed onto a piece of paper and a sheet of Mylar was laid over the pattern. The carbon fiber rods were then positioned over the Mylar according to the planform layout and attached with adhesive tape. The main reason for having the wing pattern traced on paper rather than directly on the Mylar is because of its thickness. The Mylar is so thin that it is hard to work with and it can be cut much easier with some sort of backing. After the all the rods

were securely attached, a thin line of tape was used to help reinforce the two exposed edges at the trailing edge and the wing tip to preventing them from easily tearing. The wing was then cut out and shaped with a pair of scissors

3.1.3   Testing Equipment

One of the larger pieces of test equipment for this research is a linear air bearing table. This piece of equipment has a 24" x 18" aluminum plate that is mounted on four linear air bearings which slide on two polished stainless steel rails. The air bearings are supplied compressed air and the porous bearings yield a virtually frictionless system ideal for measuring small axial loads. Due to the relatively large weight of the table compared to the flapping mechanism, the dynamic forces of the flapping motion are smoothed out and the resulting force is the average thrust over time.

In order to measure the average thrust produced the flapping mechanism, a pair of 0.5 Newton (50 grams) capacity load cells were used to measure the force. The main reason for using two load cells is the added reliability of having multiple force transducers measuring the same load, which should result in exactly the same readings. One of the load cells is an Interface ULC-0.5N force transducer and the other is a Sensotec model 31/1435-50 gram load cell manufactured by Honeywell, both shown in Figure 31.
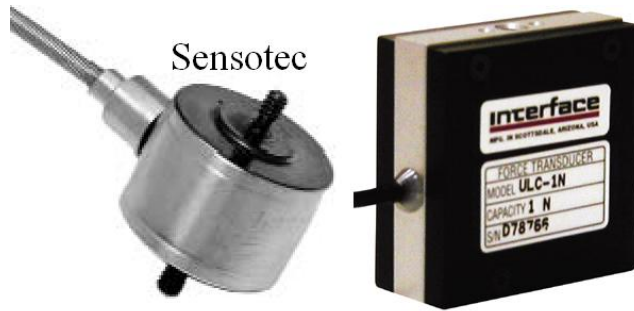
Figure 31: Sensotec and Interface Load Cells

The Interface load cell is operated by a unit that serves as the power source for the transducer as well as the display, seen in Figure 32. This module allows the user to switch between different modes of operation, along with calibrating and zeroing the force readout. The Sensotec load cell is powered by a separate AC to DC power module connected to Sensotec in-line amplifier. This amplifier also houses multiple potentiometers used for calibrating the load cell, discussed in Section 3.2. The voltage signal that is output from the amplifier is then measured using an Agilent digital multimeter.

Figure 32: Interface Load Cell Display

The mounting orientation of both loads cells is shown in Figure 33. The Sensotec load cell is fixed to the air table using an angle bracket which allows it to move with the table, while the Interface load cell is mounted in a stationary position. In order to protect the relatively fragile load cells, an adjustable stop was placed on the air table that keeps load cells from accidentally colliding into one another once the air table has been activated.
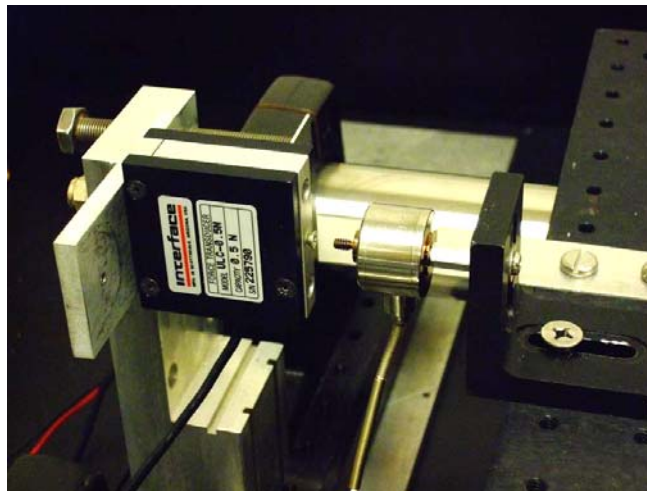
Figure 33: Load Cell Mounting Orientation

The DC electric motor used for the flapping mechanism is powered and controlled by an Instek laboratory DC power supply, shown in Figure 34. The display indicates the total amount of amps and volts being used by the motor, and whether the power supply is operating at constant current or constant voltage. This setting allows the user to adjust the maximum output of either the current or voltage to keep from exceeding the capabilities of the motor. The current and voltage are each controlled using two potentiometers with a fine and course adjustment.
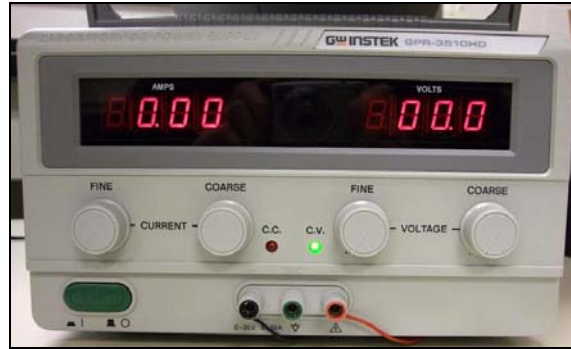
Figure 34: Instek DC Power Supply

One very helpful piece of equipment used for this research was a monarch phaser strobe. The strobe light emitted from this handheld device caused the wing to appear frozen within the flapping stroke, allowing the user to visualize the shape of the wing. This device also made it possible to measure the flapping frequency of the mechanism using an optical sensor. This optical sensor operated by detecting a small piece of reflective tape attached to the crankshaft, illustrated in Figure 35.
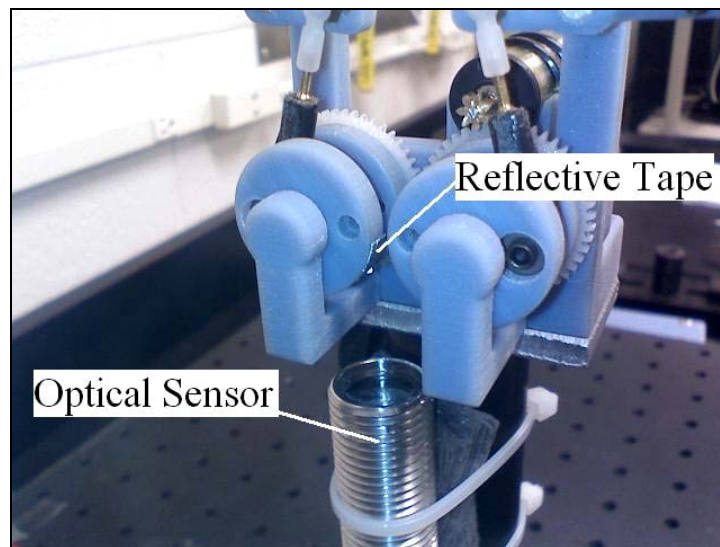
Figure 35: Phaser Strobe Optical Sensor

Every time the crankshaft completed a revolution, the reflection of the light from the optical sensor hitting the tape would trigger the strobe. The strobe also had a backlit display that would indicate the speed of the mechanism in revolutions per second (Hz). Another feature of the strobe was that it can be operated in phase delay mode, which causes the strobe to fire at some delay after the optical sensor has been triggered. This delay period could be adjusted in real-time, which allowed the user to visually freeze the wing at any given point throughout the flapping stroke.

The AFIT-2 six degree-of-freedom force balance manufactured by Modern Machine and Tool Company was used to acquire time resolved force data for multiple points throughout a flapping stroke. The balance consists of multiple strain gauges, which are a series thin wire filaments arranged in a Wheatstone Bridge configuration. The maximum load limits for the force balance are:

Table 3: AFIT-2 Force Balance Maximum Loads

Component	Maximum Load
Normal Force	4 lbs
Axial Force	2 lbs
Side Force	2 lbs
Pitch Moment	2 in-lbs
Roll Moment	4 in-lbs
Yaw Moment	2 in-lbs

The load ratings for the balance are small, leading to high accuracy. Since the balance is relatively fragile, most of the initial tests were conducted using an air bearing table and inexpensive, but accurate, load cells. The force balance was attached to a metal sting and secured to the air table with a mount fabricated on the 3-D printer, shown in Figure 36.
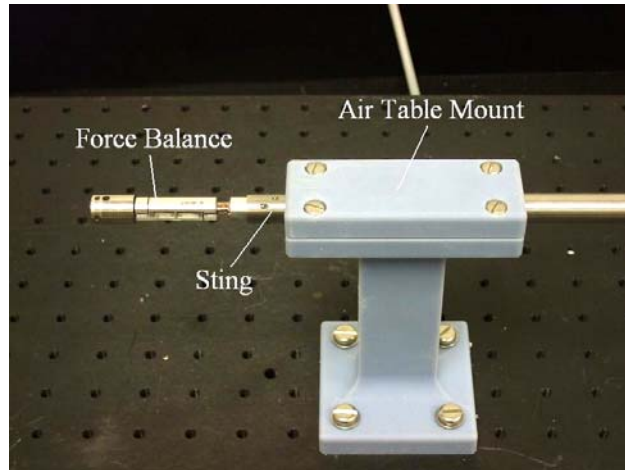
Figure 36: Force Balance Mounting Arrangement

The force balance was operated using National Instruments LabView 8.5. A

Virtual Instrument (VI) was designed that would acquire the data from the force balance

and save it to an excel spreadsheet. The VI was constructed using the block diagram

shown in Figure 37.
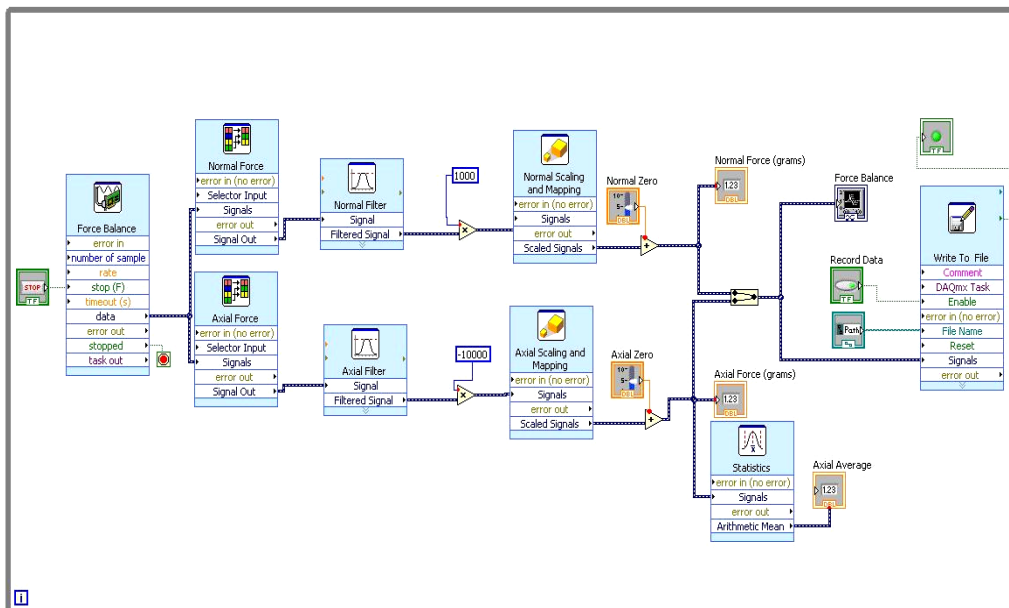
Figure 37: LabView Virtual Instrument Block Diagram

Within the block diagram was a data acquisition module that receives the complete signal from the force balance and separates it into the axial and normal force signals. The two individual signals each pass through a lowpass filter for noise reduction and a scaling function for calibration purposes. The filter settings and scaling factors are shown in Appendix C. The VI was operated with the control panel seen in Figure 38.
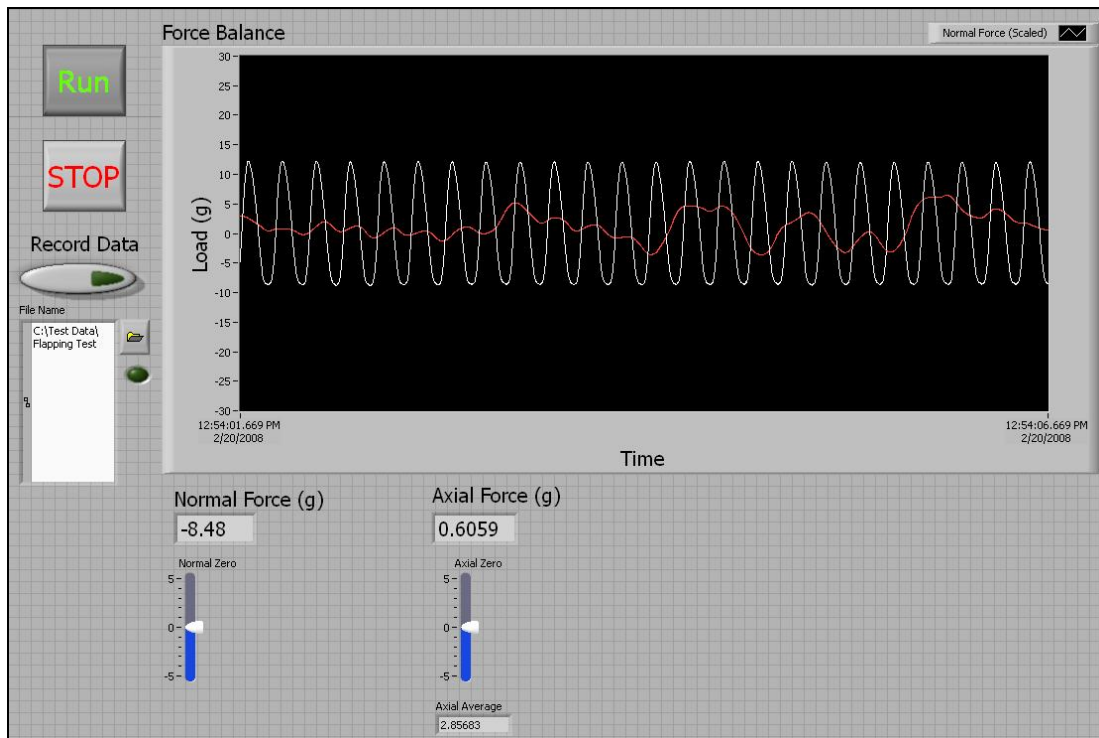
Figure 38: LabView Virtual Instrument Control Panel

The VI control panel displayed the axial and normal forces in real time on a waveform chart in units of grams. The normal and axial forces could be zeroed using two slide bars in the lower portion of the control panel before any load was applied to the force balance. Two X-Stream XS-4 high speed cameras built by Integrated Design Tools Incorporated and supplied by Dantec were used to capture high speed imagery of the

flapping mechanism in motion. The camera is controlled by a program called X Vision

that allows the user to adjust viewing area, which has a direct effect on the maximum

frame rate. The frame rates vary from 5,000 frames per second with the largest viewing

area, up to 40,000+ frames per second when the viewing area is significantly decreased.

In order to test whether or not the still images from the camera would be able to be used

for photogrammetry, a small test model was made to simulate the shape of a flapping

wing. This small model can be seen in Figure 39.
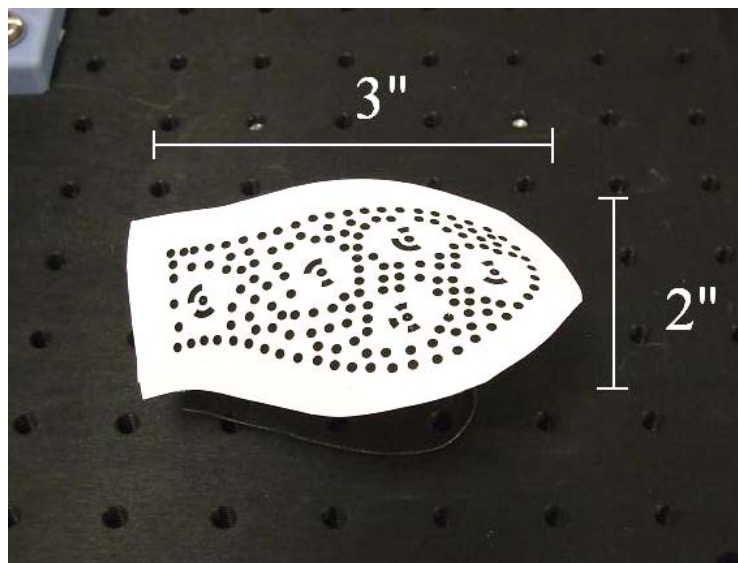
Figure 39: Mock Photogrammetry Wing Model

The wing model was covered with black target markers in a random pattern, along

with five coded targets that are automatically recognized by the photogrammetry

software. The program used for performing the photogrammetry analysis was

Photomodeler by Eos Systems Inc.

3.2   Experimental Procedure

3.2.1   *Load Cell Calibration*

Before the both of the load cells could be used for taking measurements, they first
had to be calibrated. The calibration process required a large testing frame and
deadweight hanger provided by Sensotec. The arrangement for calibrating the load cells
can be seen in Figure 40.
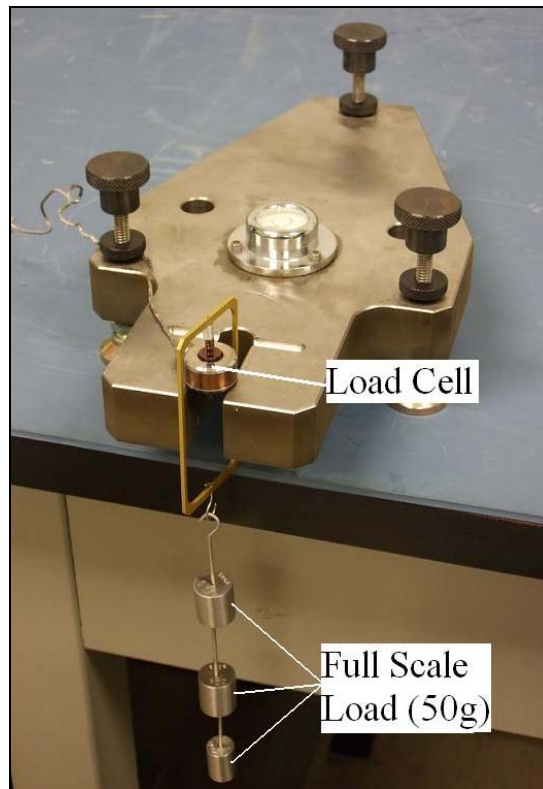
Figure 40: Load Cell Calibration Setup

The actual calibration process differs slightly for both load cells. The first step
for calibrating the load cells was to be sure that power is provided to the unit for at least

10 minutes to allow the unit to properly stabilize. For the Sensotec load cell, with zero load or pressure on the transducer, the zero potentiometers housed in the in-line amplifier were adjusted to indicate zero volts on the digital voltmeter. There are two adjustment potentiometers for course and fine tuning. Next, the full scale load was applied to the transducer and the span potentiometer was adjusted to indicate a full scale reading on the voltmeter. In this case for a 50 gram load cell (0.5 Newton), the full scale reading was 5.0 volts. The voltage reading displayed on the voltmeter can be converted to a force (grams) by multiplying the displayed voltage by a factor of ten.

The process of checking the accuracy from zero and full scale points was then repeated in 10 gram increments. The calibration sequence for the Interface load cell still requires a zero and full scale load, however, the these points were automatically set in the control unit using the calibration button.

3.2.2 Force Balance Calibration Procedure

For this research, the force balance was calibrated in the normal and axial force directions. For the normal force direction, a calibration fixture provided with the force balance was placed over the end of the balance and provided a flat surface from which weights could be placed. As with the load cells, first a zero load readout was recorded for an initial data point. After a starting point was established, weights were added in 10 gram increments up to a total load of 50 grams. The process of starting with a zero load and increasing up to 50 grams provided a linear data set, resulting in the slope of a line that could be used as the calibration factor.

This calibration factor for the normal force direction was entered into the scaling and mapping function within LabView virtual instrument block diagram in the form of an equation of a line. This calibration process was repeated for the axial force direction with the force balance positioned vertically with weights placed on top of the calibration fixture.

3.2.3 Air Bearing Table

The air bearings must be connected to a dry air supply source to avoid clogging the air bearings with any type of moisture. For this research, the table was connected to a 120 pounds per square inch (psi) air supply regulated to 80 psi. The table itself must be placed on a very flat and rigid surface since even the slightest movement can affect the results. The table has adjustable bolts on each of the four corners that were used for leveling the system.

In order to conduct the thrust measurements, the load cells must be preloaded to 30 grams. This requires that the load cells be zeroed, and the table was angled ever so slightly by unscrewing the leveling bolts at the head of the table until the load cells were touching. Preloading was necessary to keep contact between the load cells and provide a zero point to start the testing. Preload also helped to counteract the oscillating type of motion that occurs whenever a new load is applied to the table. This oscillating motion was critical to the accuracy of the measurements and must be settled before the load cells could be zeroed. An acceptable margin for these oscillations was when the readout varied less than ±0.02 grams. Once the load cells had been preloaded and table was settled, the load cells were zeroed once again and the testing commenced.

3.2.4 Thrust Measurement Procedure

After mounting the pair of wings onto the flapping mechanism, the testing began. The motor was operated using the DC power source and controlled using the fine and course voltage knobs. In order to operate the power supply in constant voltage mode, the course adjustment for controlling current was turned all the way on and confirmed by the illumination of the constant voltage light. The flapping speed was checked with the phaser strobe and adjusted to the correct speed using the voltage control.

Once the desired flapping rate was achieved, the table had to settle before readings were taken. The table had settled to an acceptable amount once measurements from the load cells are only varying by less than ±0.05 grams. After the table has settled, the phaser strobe was checked one last time to ensure the flapping mechanism was operating at the desired speed. The thrust measurement was then recorded in an Excel spreadsheet. The configuration of the flapping mechanism for thrust measurements can be seen in Figure 41.
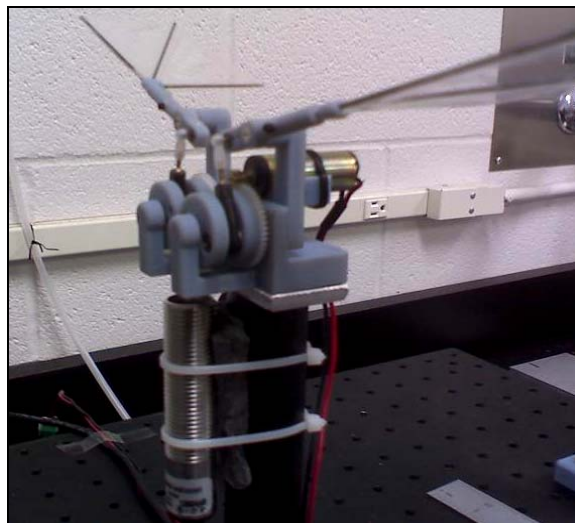
Figure 41: Air Bearing Table Mounting Configuration

The method for calculating the thrust coefficient varied slightly from the equation presented in Section 2.2 which accounted for the forward flight velocity. Since the flapping mechanism was stationary without any forward motion, the thrust coefficient was calculated using Equation 4.

$$C_t = \frac{T}{\rho n^2 D^4} \tag{4}$$

where

T = thrust force (Newtons)

ρ = local air density (kg/m^3)

n = flapping speed (Hz)

D = wing span (m)

In addition to the coefficient of thrust, the coefficient of power for each test was calculated using Equation 5. This equation uses the same variables as the thrust coefficient equation, with the exception of the power term.

$$C_{p,m} = \frac{P_m}{\rho n^3 D^5} \tag{5}$$

where

P_m = Power supplied to the motor (watts)

A figure of merit for each wing was calculated using Equation 6 (Noonan, 2001). This equation was adapted from rotorcraft application as a means of quantifying performance.

$$FM = \frac{C_t^{3/2}}{\sqrt{2}C_{p,m}}$$ (6)

3.2.4 Force Balance Procedure

Taking measurements with the force balance began with opening the virtual instrument in LabView 8.5. This virtual instrument used a National Instruments SCXI-1314 Universal Strain Terminal Block to provide power to the force balance along with acquire the data. Once the virtual instrument was running, the process of setting the flapping mechanism to the desired speed was the same as in the thrust measurement procedure. Within the virtual instrument there was a dialogue box to enter the desired location and file name to save the test data. Once the virtual instrument was running and the flapping mechanism was operating at the correct speed, the data set was recorded to an Excel spreadsheet. The configuration of the flapping mechanism for the force balance can be seen in Figure 42.
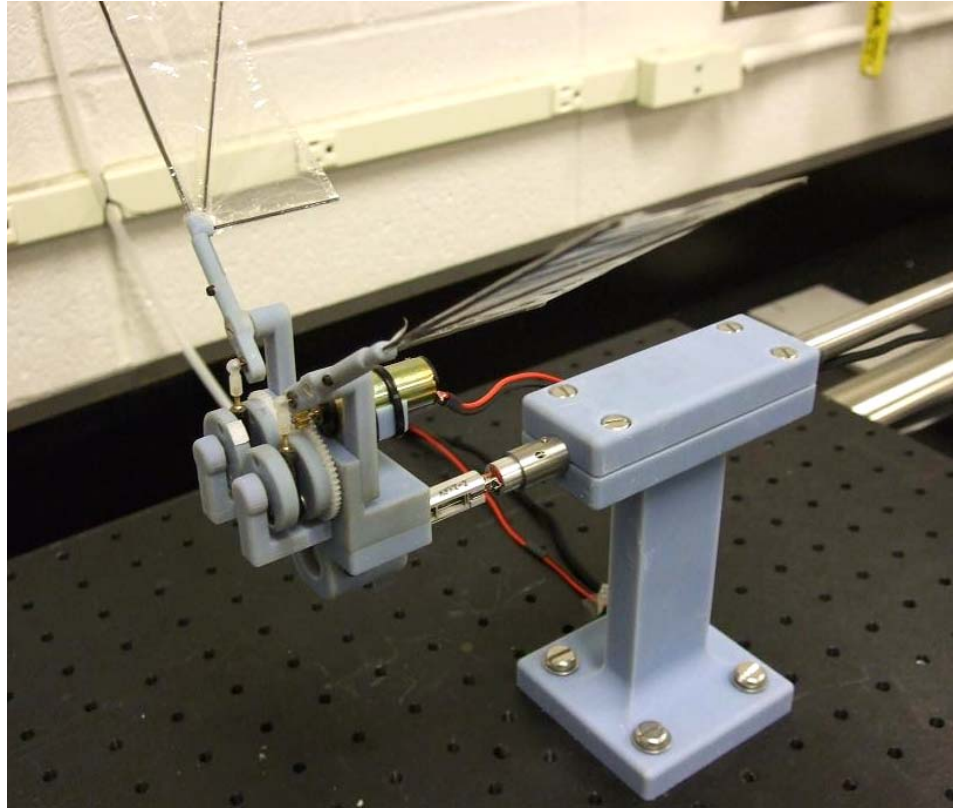
Figure 42: Force Balance Mounting Configuration

3.2.5   *High Speed Camera / Photogrammetry Procedure*

The high speed cameras were positioned so they would view the wing during the upper half of the flapping stroke. The orientation of the cameras with respect to the model can be seen in Figure 43.
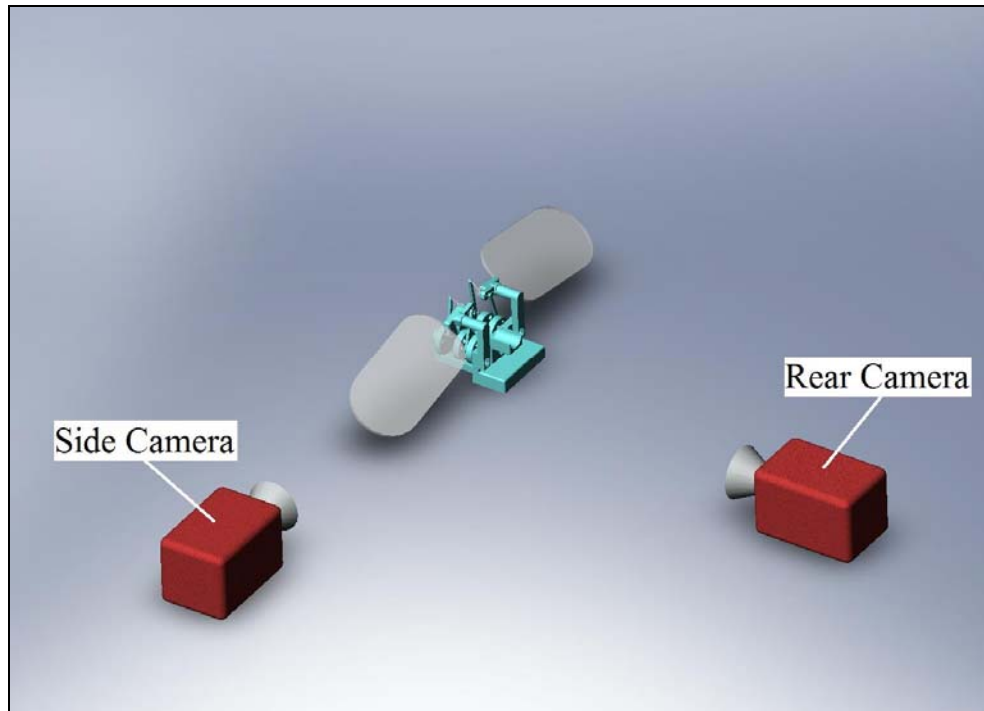
Figure 43: High Speed Camera Orientation

In order to analyze how the shape of the wing changed at higher flapping frequencies, video taken at two different flapping speeds is compared for each wing configuration. Pictures from all four sides of a calibration grid were then taken using the same high speed cameras. These pictures were then loaded into Photomodeler where the program automatically determined camera parameters. Pictures of the mock wing were taken with the high speed camera from four different angles and opened with Photomodeler. The program automatically correlated the wing within each of the individual pictures using automated target markers. Once the program solved for the position and orientation of the wing, a 3-D model of the shape of the wing was constructed.

3.2.5 Testing Scenarios

The testing scenarios were primarily designed to verify the capabilities of the testing equipment and the best method to obtain accurate measurements. The primary test subjects were the four wing configurations with a span-to-chord ratio of 2:1. All of these wings were designed to operate at different flapping speeds, which can be seen in Table 4 below:

Table 4: Wing Flapping Speeds

Wing Size	Flapping Speed (Hz)
#1 – 4" x 2", 12.1" Span	3.5 - 7.5
#2 – 3.5" x 1.75", 11.1" Span	5 – 9
#3 – 3" x 1.5", 10.1" Span	7 - 11
#4 – 2.5" x 1.25", 9.1" Span	8 - 15

The flapping speed for configuration #1 was incremented in 0.5 Hz steps, and configurations #2-#4 were 1 Hz increments. The lowest flapping speed for each set of wings was determined from when they produced between 0.5 and 0.7 grams of thrust. The maximum flapping rate for each configuration was the point where the flapping mechanism could be operated without the risk of permanently damaging the wing membrane material. Each set of tests was conducted a total of 20 times to gather a large number of data points and to determine the repeatability of each testing condition.

Overall, Chapter 3 detailed the design and construction of the flapping mechanism and wings used for testing. A description of the testing equipment was given along with the procedures followed for load cell calibration, thrust and normal force measurements, and high speed camera operation. The next chapter will present the results from this testing.

4. Results

4.1 Thrust Measurements

As mentioned in Chapter three, the first series of tests for this research was to gather data regarding the accuracy of the thrust table along with the performance of the Mylar and carbon fiber wings. The initial experiment runs were conducted with the 4" x 2" wing configuration under the conditions shown in Table 4. The results from these tests can be seen in Figure 44.
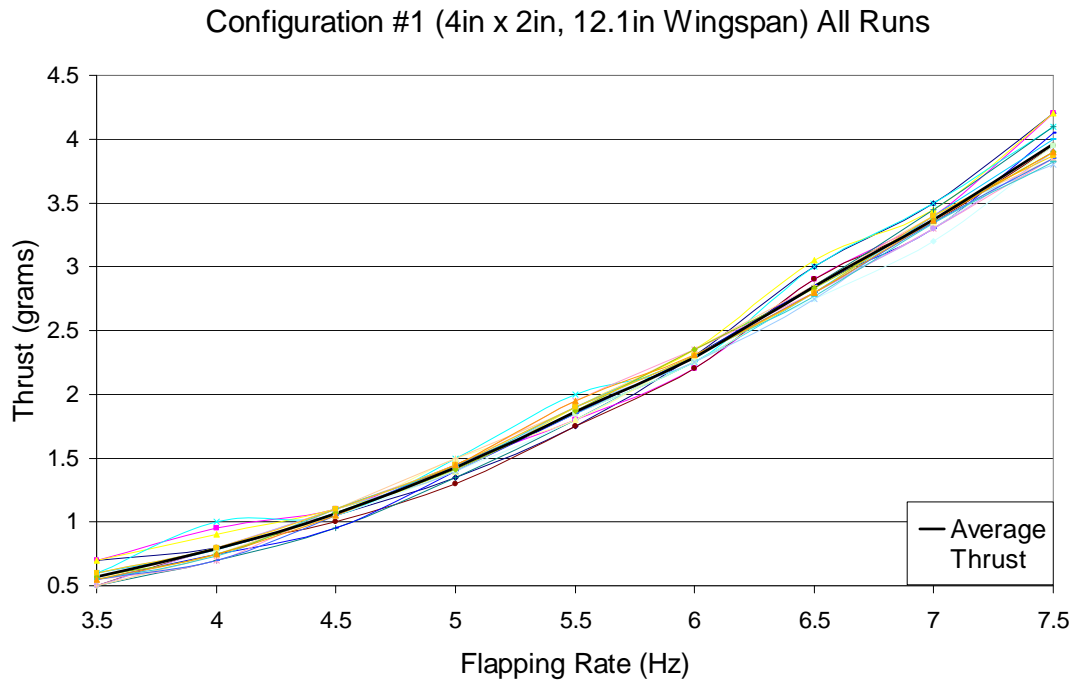
Figure 44: 4" x 2", 12.1" Span Wing Thrust Data

Each of the colored lines represents an individual test, with the average of all 20 runs shown as the solid black line. At the slower flapping speeds (3.5 – 4 Hz) there was a

larger deviation in the data between the minimum and maximum thrust readings for the

20 separate tests. This variation can largely be attributed to the fact that the oscillations

of the air table were more prevalent at these lower flapping speeds, affecting the

consistency of the measurements less than one gram. The data collected at the 7.5 Hz

flapping speed also proved to be less repeatable, possibly due to the physical deformation

of the wing. It may have been beneficial to determine at what speed the thrust begins to

decrease, however, this would have exceeded the capabilities of the Mylar wing

membrane. The second testing configuration was the 3.5" x 1.75" wing, and the results

can be seen in Figure 45.
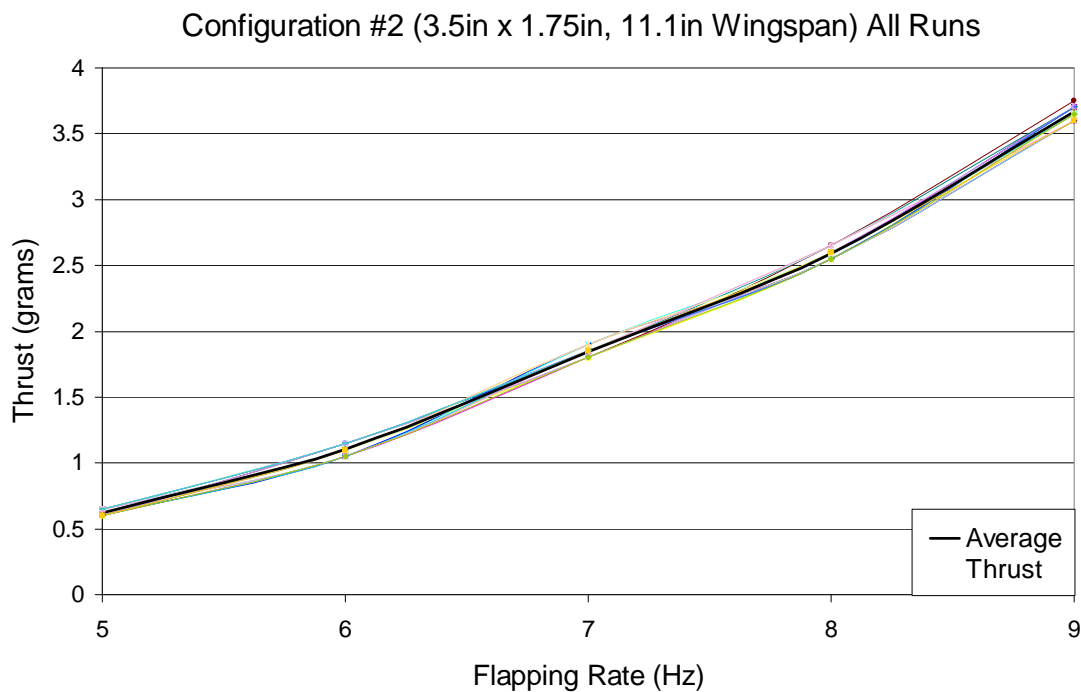
Figure 45: 3.5" x 1.75", 11.1" Span Wing Thrust Data

This configuration had more consistency between each of the runs, with less

variation in the final measurements than configuration #1. This set of wings also had a

slightly lower maximum thrust than the first configuration, which may be attributed to the smaller planform area of the wings. This lower thrust may also be a result of varying aeroelastic effects between the two different wings sizes. The results from the third testing configuration can be seen in Figure 46, performed with the 3" x 1.5" wings.

Configuration #3 (3in x 1.5in, 10.1in Wingspan) All Runs
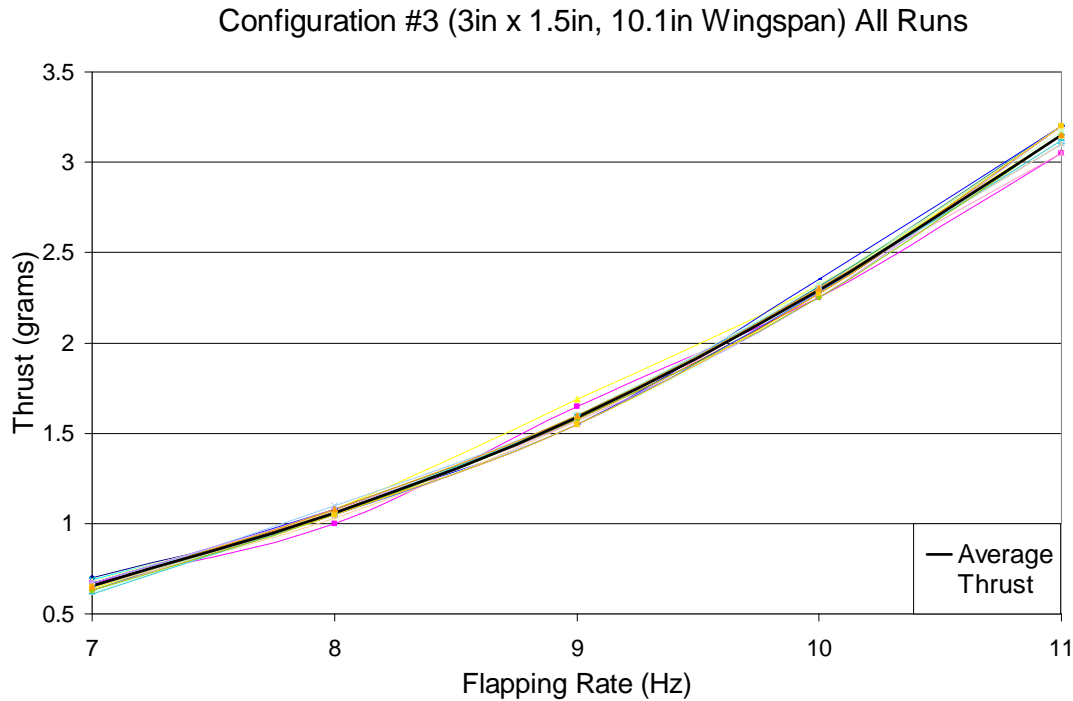
Figure 46: 3" x 1.5", 10.1" Span Wing Thrust Data

As seen with the data from the second configuration, the data for this set of tests was consistent between each of the runs. The standard deviation for the 3" x 1.5" wings ranged from 0.022 grams at 8 Hz, which was the lowest deviation for all four configurations, to 0.051 grams at the maximum 11 Hz flapping speed. The results from the fourth and final wing configuration are shown in Figure 47.

Configuration #4 (2.5in x 1.25in, 9.1in Wingspan) All Runs
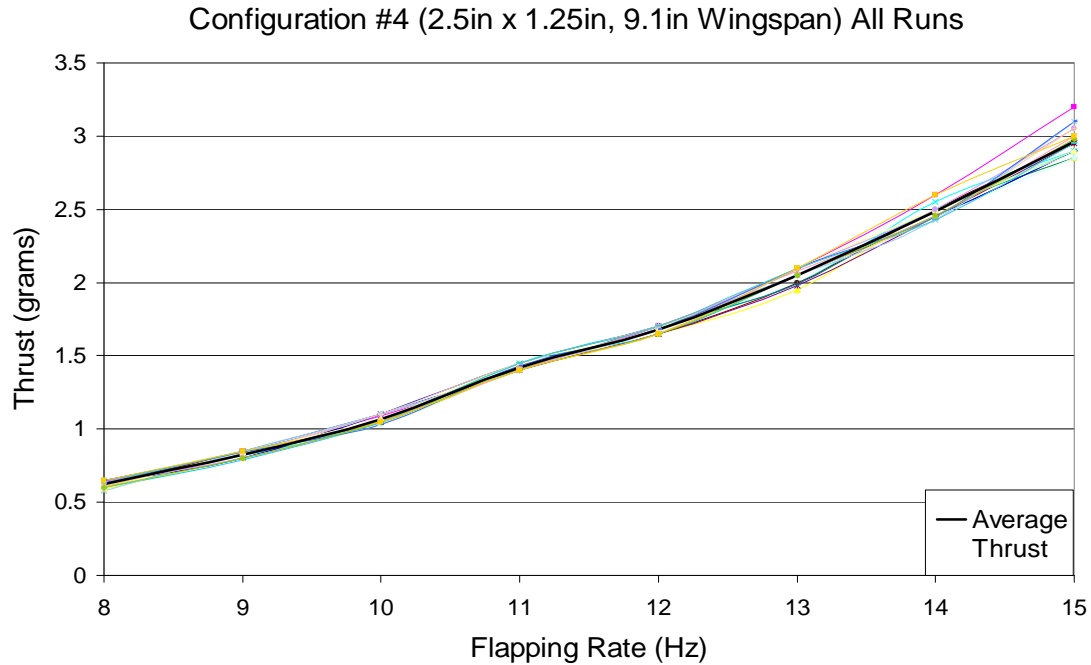
Figure 47: 2.5" x 1.25", 9.1" Span Wing Thrust Data

As seen in Figure 47, the data at the highest flapping speed began to become more widely separated between runs, similar to the 4" x 2" wing configuration from the first testing scenario. After the 20 test runs were conducted, the standard deviation of the thrust measured for each flapping speed could be calculated, shown in Table 5.

Table 5: Standard Deviation for Thrust Measurements (20 Runs)

Flapping Speed (Hz)	4 x 2 Wing 12.1" Span (g)	Flapping Speed (Hz)	3.5 x 1.75 Wing 11.1" Span (g)	Flapping Speed (Hz)	3 x 1.5 Wing 10.1" Span (g)	Flapping Speed (Hz)	2.5 x 1.25 Wing 9.1" Span (g)
3.5	0.066	5	0.026	7	0.023	8	0.023
4	0.079	6	0.041	8	0.022	9	0.023
4.5	0.048	7	0.036	9	0.035	10	0.027
5	0.052	8	0.038	10	0.027	11	0.023
5.5	0.067	9	0.043	11	0.051	12	0.023
6	0.045					13	0.046
6.5	0.085					14	0.050
7	0.073					15	0.096
7.5	0.133						

The relatively low standard deviation for each data set implies that all of the thrust tests are very repeatable, with only minor variation in the thrust measurements between tests. The raw data for each test can be seen in Appendix A. A comparison of the average thrust from each configuration can is shown in Figure 48. In the legend for the plot, "b" refers to the total wingspan and "w" is the chord length for each configuration.
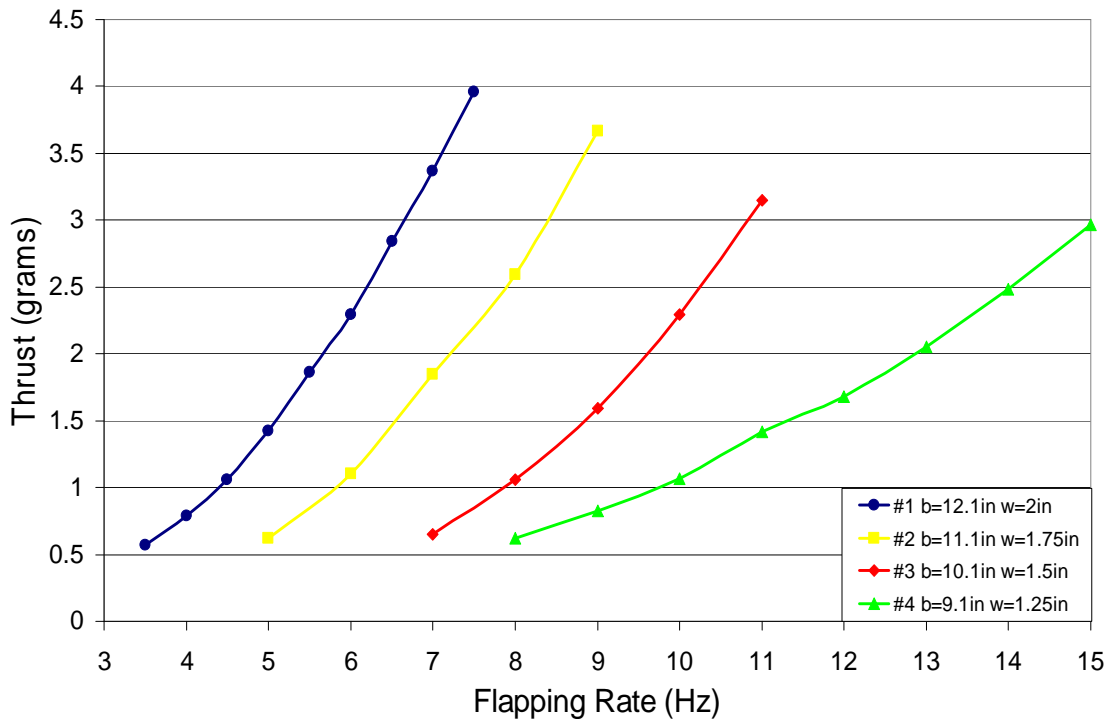
Figure 48: Flapping-Wing Average Thrust Comparison

The figure above shows how the maximum thrust decreased for decreasing planform area. It also illustrates how the smaller wings can operate over a wider range of flapping rates before exceeding the capabilities of the flapping mechanism. The thrust coefficients were also calculated for each configuration, which can be seen in Figure 49.
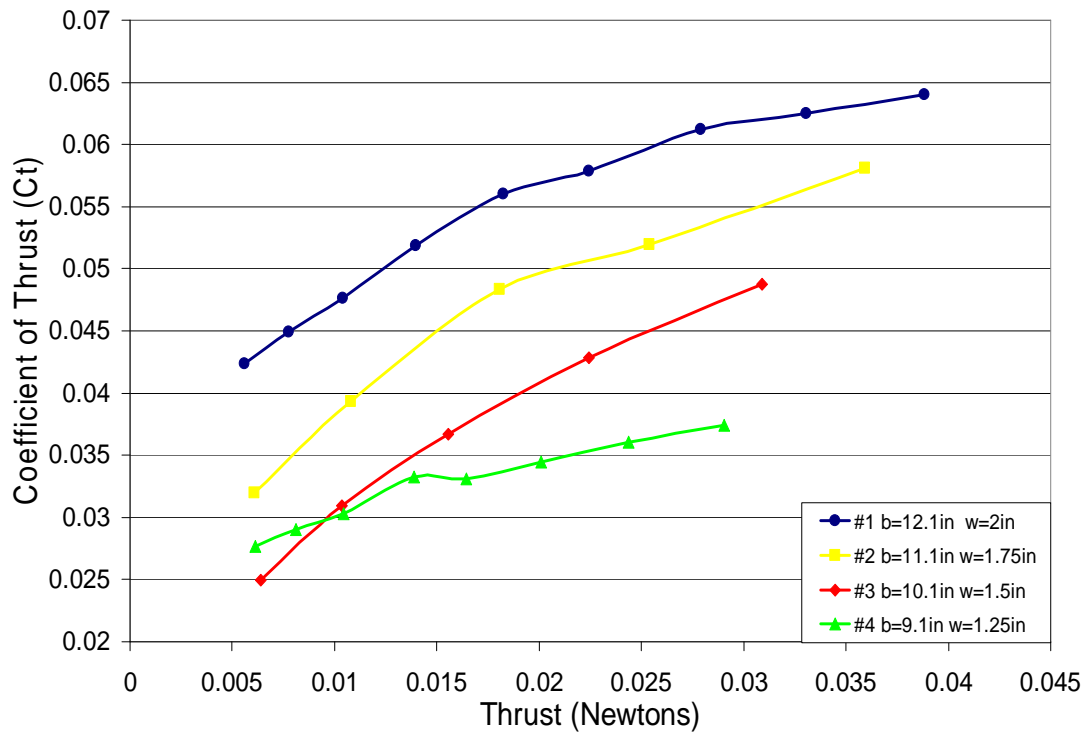
Figure 49: Flapping-Wing Thrust Coefficient Comparison (vs. Thrust)

The thrust coefficient for the smallest wing configuration (9.1" span and 1.25" chord) varied slightly when compared to the other three wing sizes. At the slowest flapping speed, the fourth configuration had a higher thrust coefficient than the third configuration since the smaller 9.1" wing produced the same amount of thrust with only a single hertz increase of the flapping speed. The equation for the coefficient of thrust has the wingspan raised to the fourth power in the denominator, which is generally the determining factor for wings of similar performance. Another plot showing the thrust coefficient versus speed is shown in Figure 50.

62
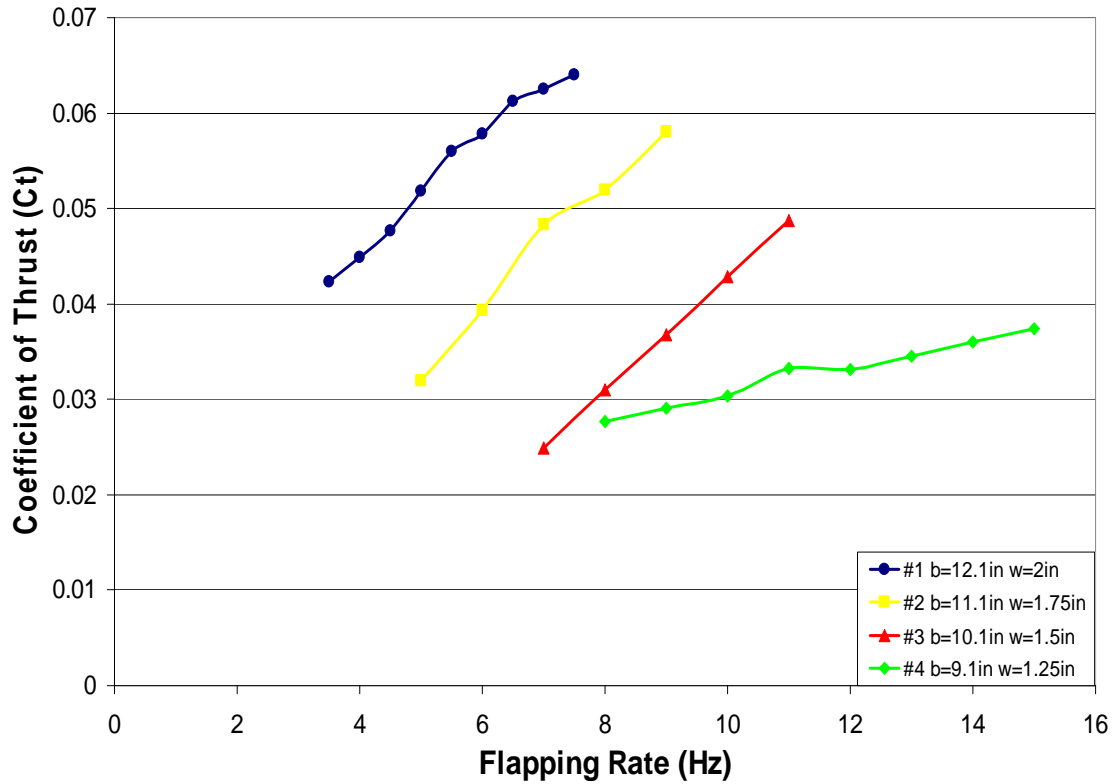
Figure 50: Flapping-Wing Thrust Coefficient Comparison (vs. Flapping Rate)

It is interesting to note that the coefficient of thrust for the third wing configuration resulted in a linear relationship when compared against the flapping rate. The amount of electrical power used by the flapping mechanism was also recorded for each testing condition, and can be seen in Figure 51. The display of the DC power supply indicated the voltage and amperage being supplied to the motor, which were multiplied together to determine the total wattage of the system.
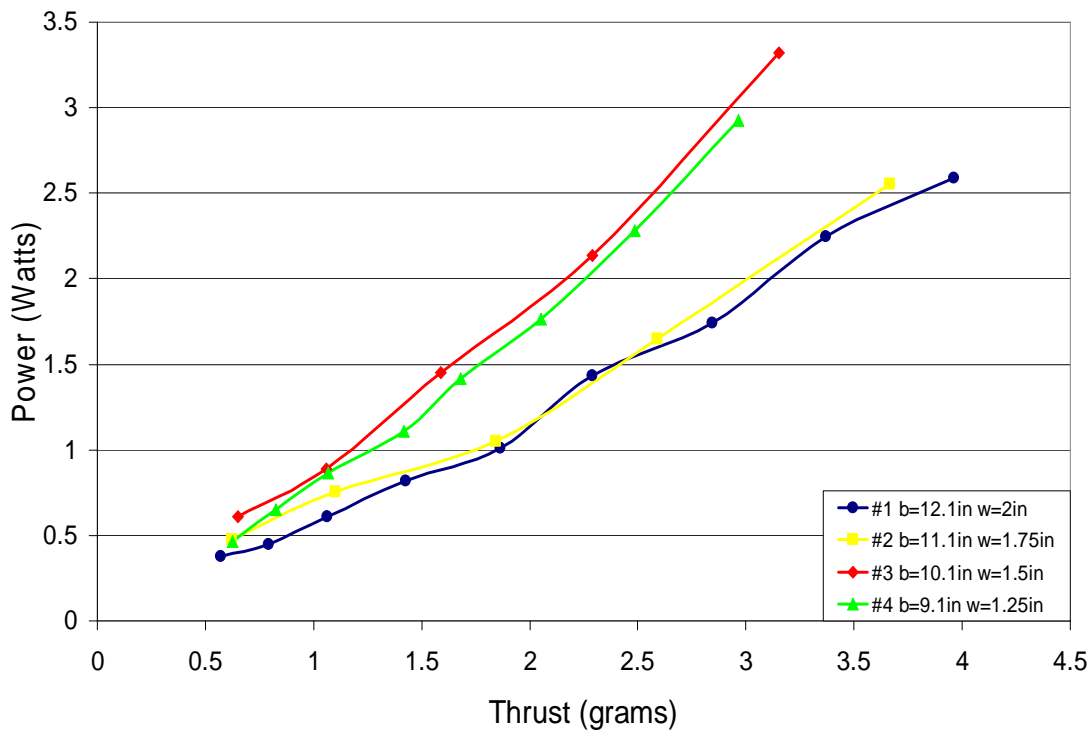
Figure 51: Flapping-Wing Power Required Comparison

When comparing the power required for all configurations, it is clear that the two
larger sets of wings (4" x 2" with 12.1" span and 3.5" x 1.75" with 11.1" span) required
less power to produce the same amount of thrust as the smaller wings. However,
flapping at the higher frequencies of the third and fourth configurations may have caused
more friction within the drive system of the flapping mechanism, resulting in the
additional power consumption. The additional power consumption may also be
associated with the inertial forces from the smaller wings changing direction more
frequently, possibly putting a larger strain on the motor. The coefficient of power was
also calculated for each configuration, which can be seen in Figure 52.
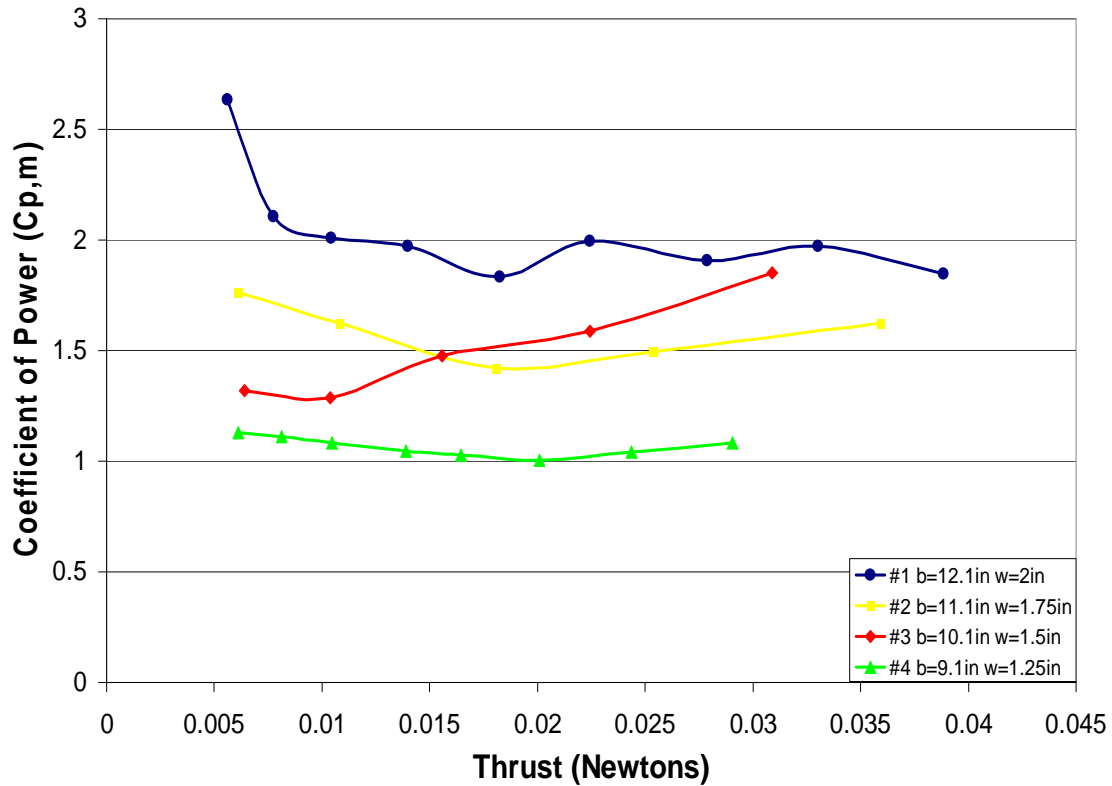
Figure 52: Flapping-Wing Power Coefficient Comparison

These coefficients of power are motor specific and are calculated based on the electrical power supplied to the motor. All of the wings have a fairly constant coefficient of power for increased thrust, except for the third configuration. The power coefficient for the 10.1" wingspan configuration appears to increase with thrust. This increased power coefficient is most likely related to the fact that the third configuration had the highest total power consumption. The final plot for the four different wing configurations is the figure of merit for each wing, shown in Figure 54. A plot showing a comparison of the coefficient of power with the coefficient of thrust can be seen in Figure 53.
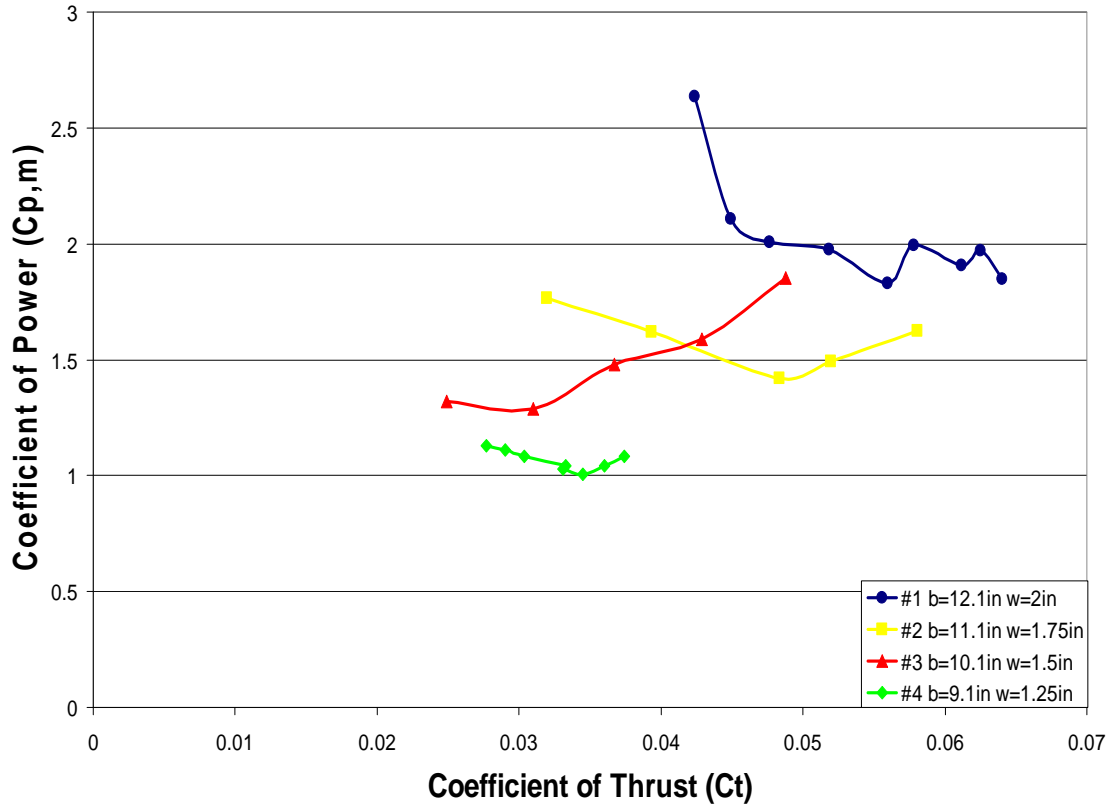
Figure 53: Flapping-Wing Coefficient of Power vs. Coefficient of Thrust

This particular plot displays the coefficient of power in relation to the coefficient of thrust, which shows similar trends for each configuration when compared to the power coefficient vs. thrust plot. Even though the thrust coefficients are rather low for these tests, the main idea behind calculating these numbers is testing whether or not it is possible to compute these parameters for different testing scenarios and wing configurations. This figure of merit was calculated according to Equation 5 discussed in Section 3.2.4.
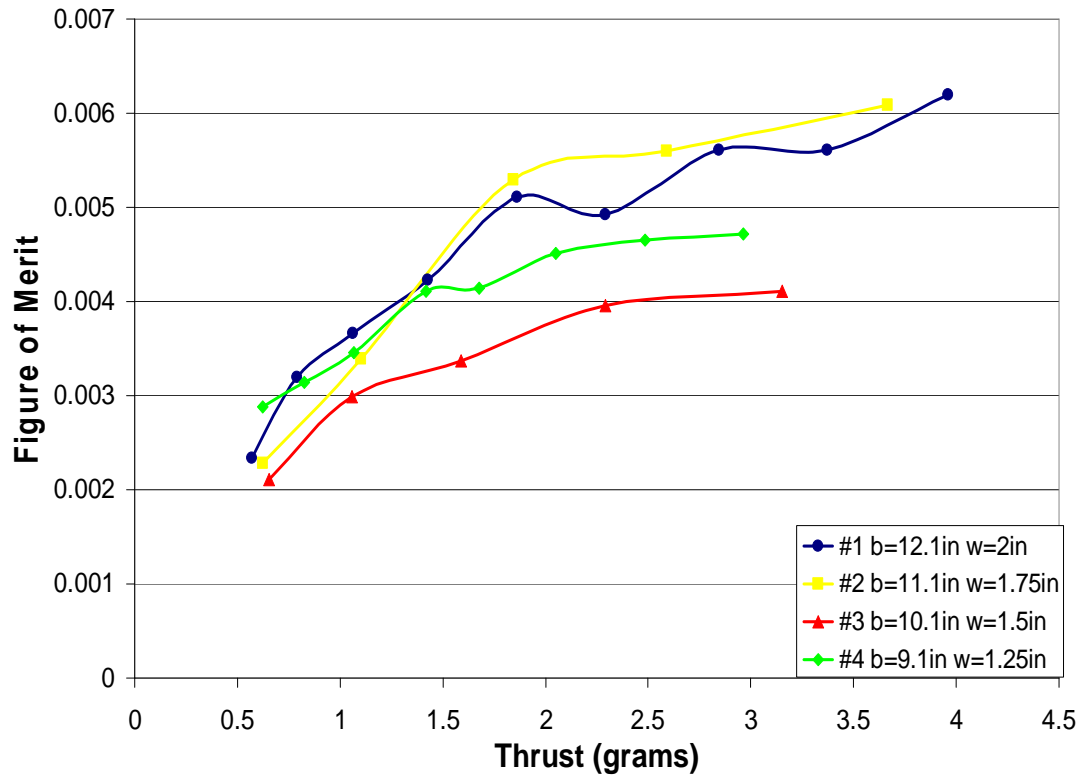
Figure 54: Flapping-Wing Figure of Merit

As with the thrust coefficients previously calculated, the figure of merit for each configuration is relatively low. The purpose of this testing was not to optimize a design that would result in the highest figure of merit, but to show that calculating this parameter is possible for flapping-wing MAVs. The second series of tests involved comparing the 4" x 2", 12.1" wing span configurations constructed with spars of different diameters. The larger carbon fiber wing spars were 0.04 inches in diameter, and the smaller spars were 0.02 inches. The smaller diameter rod was more elastic, allowing for a more flexible wing while flapping. The average thrust comparison between the two wings with different size wing spars can be seen in Figure 55.
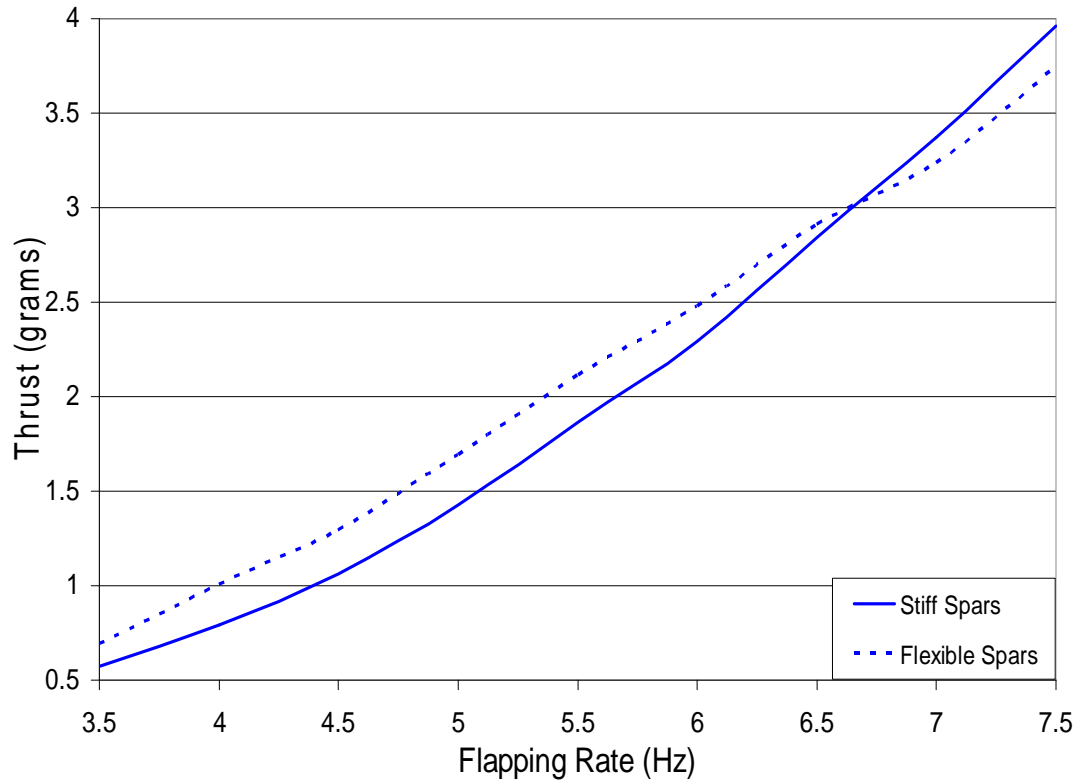
Figure 55: Stiff vs. Flexible Spars Thrust Comparison (4" x 2", 12.1" Span Wing)

From the data collected for the two different spar thicknesses, the more flexible spars resulted in a higher thrust until the 6.5 Hz range. After this point, the wing with the thicker spars proved to have a higher average thrust. This slight decrease in the slope of the thrust of the more flexible wing at higher frequencies may be related to wing deformation, resulting in a lower thrust than the stiffer wing. This result for the more flexible wing is consistent with the research conducted by Ho at the University of California, Los Angeles and Wilson and Wereley at the University of Maryland discussed in Section 2.2. The power consumption of the two wings was also compared, shown in Figure 56.
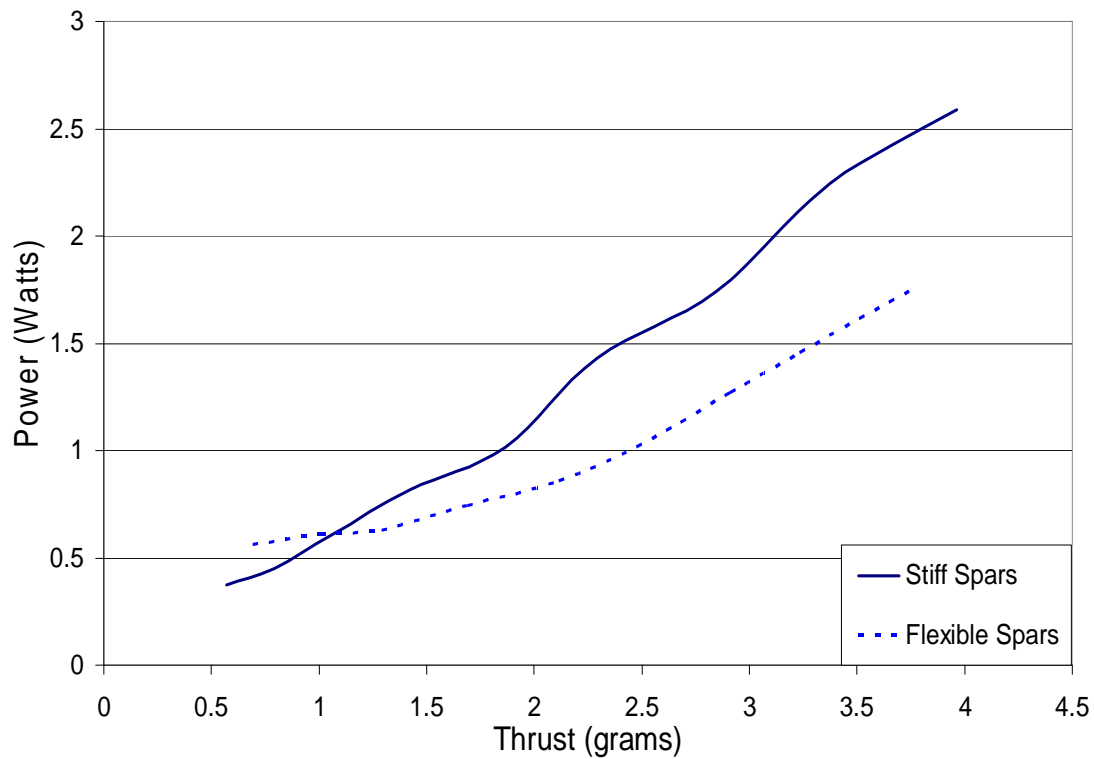
Figure 56: Stiff vs. Flexible Spars Power Required (4" x 2", 12.1" Span Wing)

It is clear from Figure 56 that the wing made with the more flexible spars required less power to operate under the same testing conditions. The higher inertia associated with the larger diameter spars may have played a role in the additional power required at higher frequencies. As the frequency increased for the stiff wing, the heavier spars may have put more strain on the motor when the wing changed direction at the top and bottom of each flapping stroke. As with the four different sized wing configurations, the figure of merit between the stiff and flexible wings is compared in Figure 57.
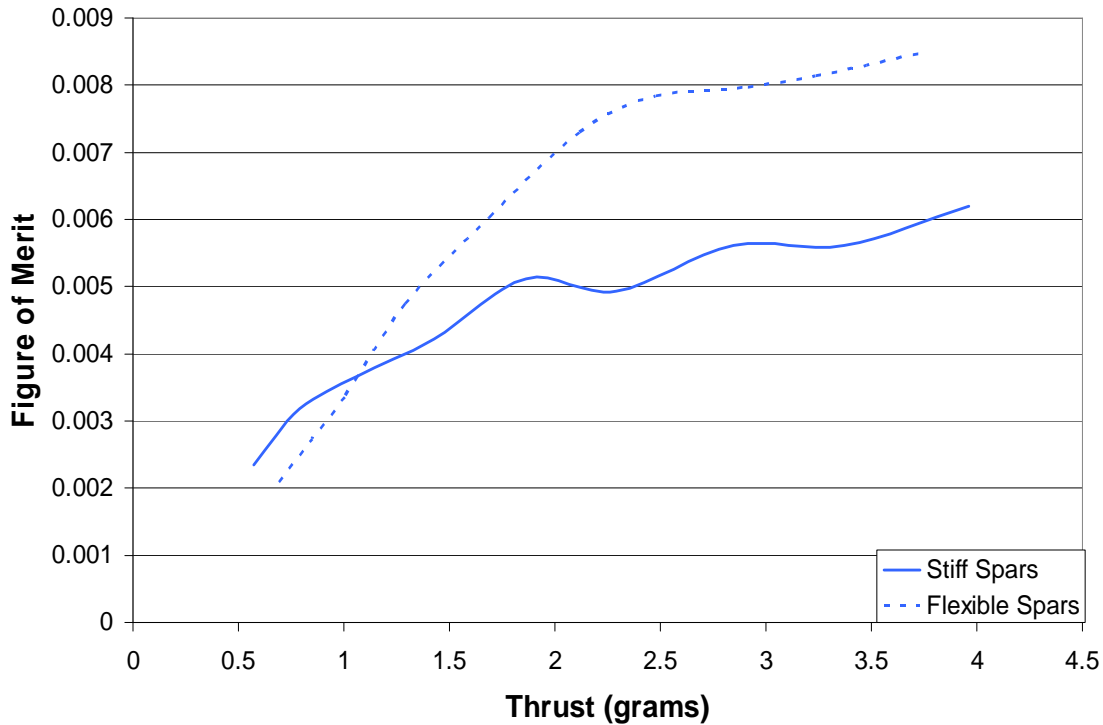
Figure 57: Stiff vs. Flexible Spars Figure of Merit (4" x 2", 12.1" Span Wing)

4.2   Force Balance Measurements

Measurements of the normal and axial forces produced by the flapping mechanism were recorded in real time using the six degree-of-freedom force balance. The wings used while collecting these measurements were the 4" x 2" wings, one set made with flexible spars and the other with rigid spars. Both sets of wings were tested at 4 and 7.5 Hz flapping frequencies, and the normal force was compared for each speed. The data for each of these tests was taken at an acquisition rate of 500 Hz.   The LabView software exports the collected data into a text file, which can be analyzed and plotted using Microsoft Excel. Data from the first set of tests ran at 4 Hz can be seen in Figure 58.
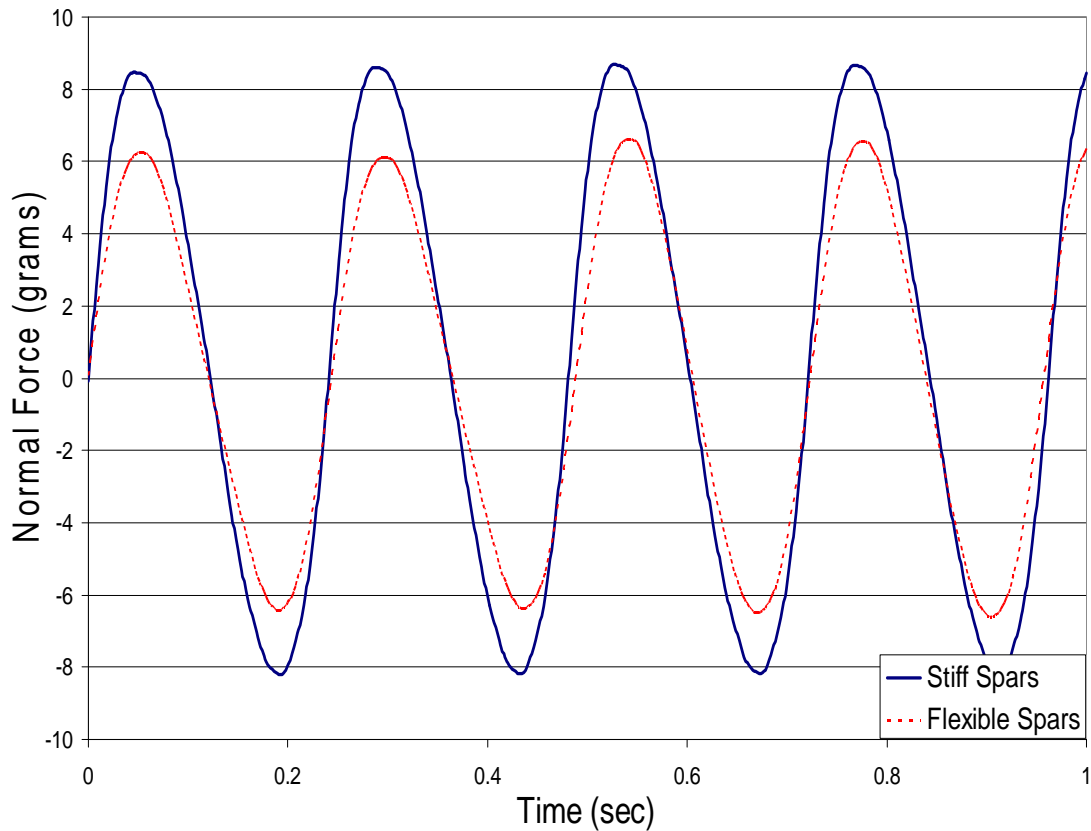
Figure 58: Stiff vs. Flexible Spars Normal Force (4 Hz, 4" x 2", 12.1" Span Wing)

The solid blue line represents the normal force recorded from the balance for the wings fabricated with the rigid carbon fiber spars, and the dashed red line is the more flexible spars. Since the wings were mounted without angle of attack, the resulting lift force (normal force) averages to zero. One possible reason for the larger maximum and minimum normal forces recorded for the stiffer wing is the added inertial forces incurred with the larger diameter spars. The added weight of these spars may induce more force as the wing continually changes flapping direction. Data collected from the 7.5 Hz test is shown in Figure 59.
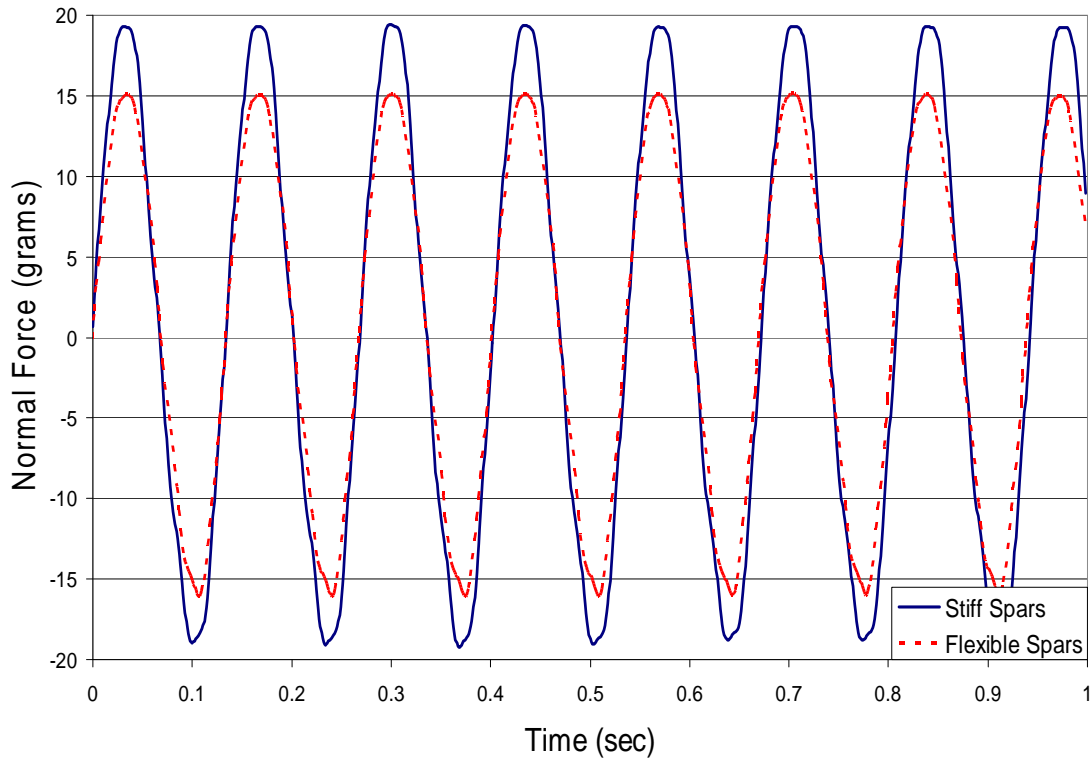
Figure 59: Stiff vs. Flexible Spars Normal Force (7.5 Hz, 4" x 2", 12.1" Span Wing)

As was the case with the 4 Hz test, the wing with the stiff spars led to a larger peak maximum and minimum normal forces recorded using the balance. In order to help understand the inertial forces associated with the flapping mechanism, the 4 and 7.5 Hz tests were repeated with the wings removed. A plot showing the normal forces produced solely by the flapping mechanism with the wings removed can be seen in Figure 60.
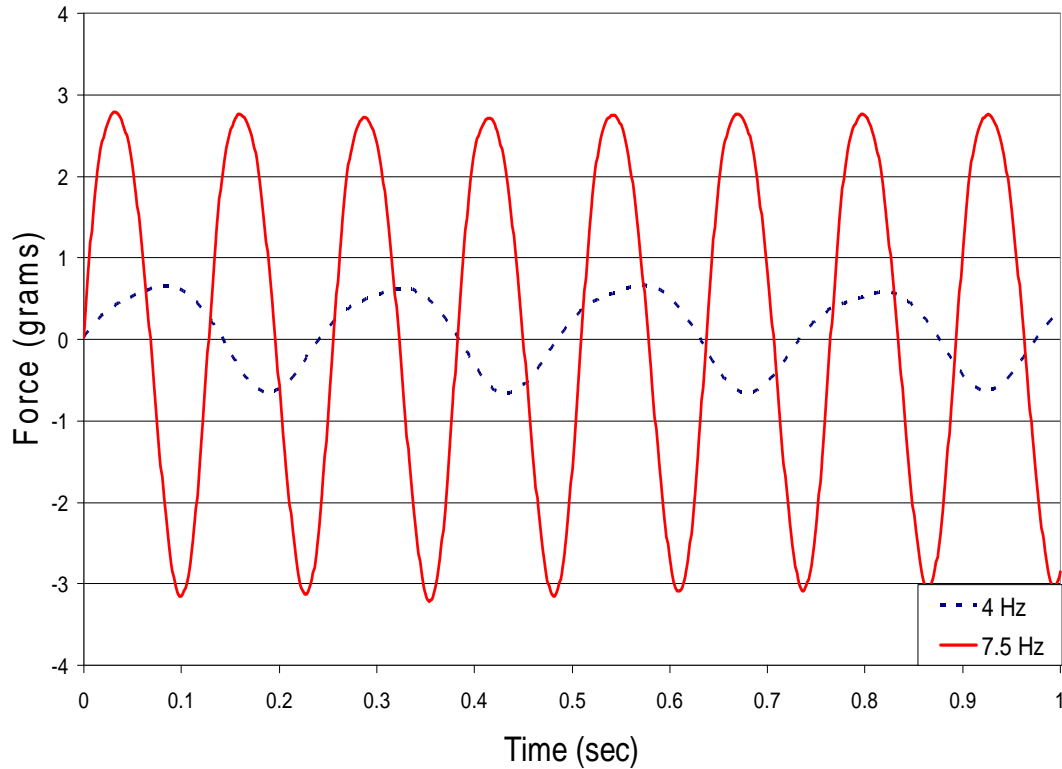
Figure 60: Inertial Normal Force of Flapping Mechanism (Wings Removed)

This plot gives an idea of the inertial forces created by the flapping mechanism, though the wings could also contribute slightly to the inertial loads. This data can be used to better estimate the total normal force produced by the flapping motion of the wings by subtracting out the normal force produced by the flapping mechanism at that given speed. The second load measured by the balance was in the axial direction, giving the thrust of the flapping mechanism. Throughout testing, the resulting axial loads measured for each of the individual runs produced data that was apparently random in nature and inconsistent with the previous thrust data collected using the air bearing table. An example plot of the axial loads measured by the force balance for the flapping mechanism with the wings removed can be seen in Figure 61.
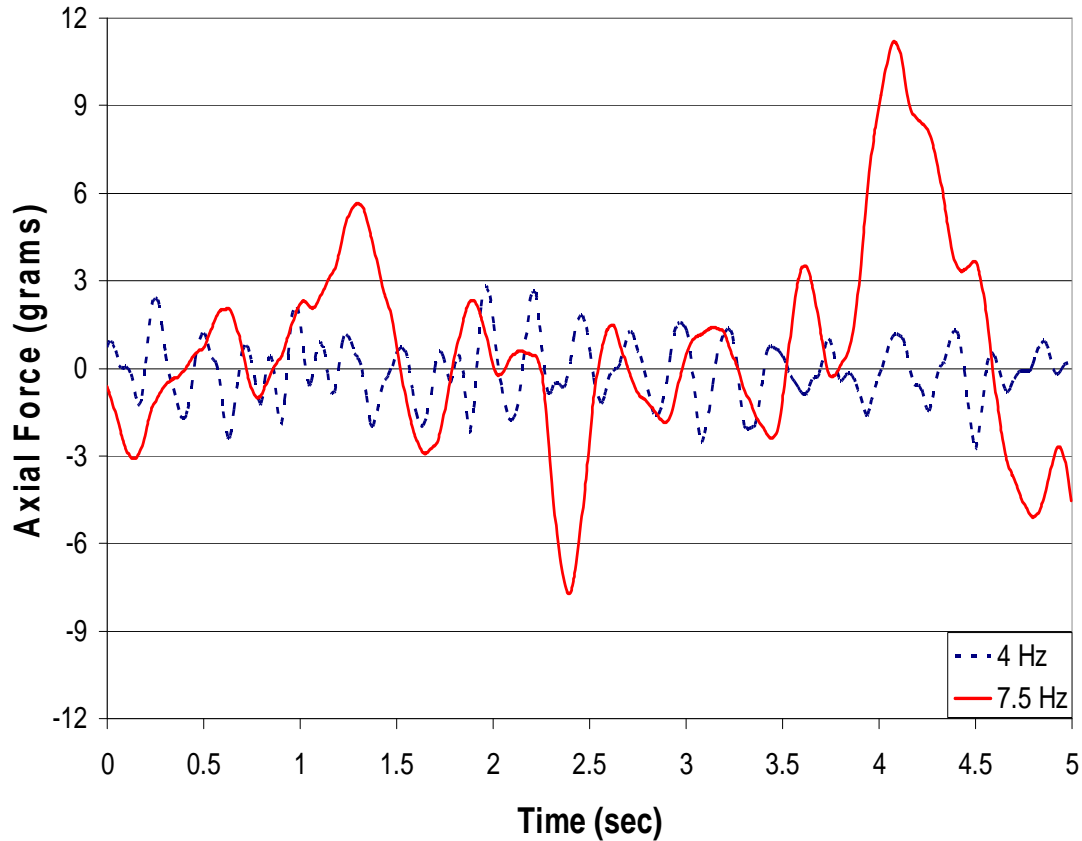
Figure 61: Axial Load of Flapping Mechanism (Wings Removed)

It is apparent from this plot that there is an error with the measurement of the axial force, particularly since at certain points (@7.5 Hz, 4 sec ~ 11g) the magnitude of the axial force is 3 times larger than the normal force for the same testing conditions. At this point in the research it is unclear as to the source of the error in the axial signal, whether it is noise in the signal itself or possibly vibrations of the flapping mechanism. One possible recommendation would be to change the orientation of the flapping mechanism on the balance, where the axial force (thrust) would then be measured as the normal force (lift). This movement would help to isolate the problem too the flapping mechanism or the balance.

4.3   High Speed Imagery

High speed imagery was a useful tool in visualizing how the stiff and flexible wings behaved at different flapping frequencies. As with the six component force balance, both sets of wings were ran at 4 Hz and 7.5 Hz. The two high speed cameras were operated at 1500 frames per second. An image of the wing during the down stroke was taken for both wing configurations to compare the overall shape of the wing. The two cameras were positioned so that one was off the left wing looking horizontally and the other directly behind the flapping mechanism. The first set of images taken at 4 Hz can be seen in Figure 62 and Figure 63.
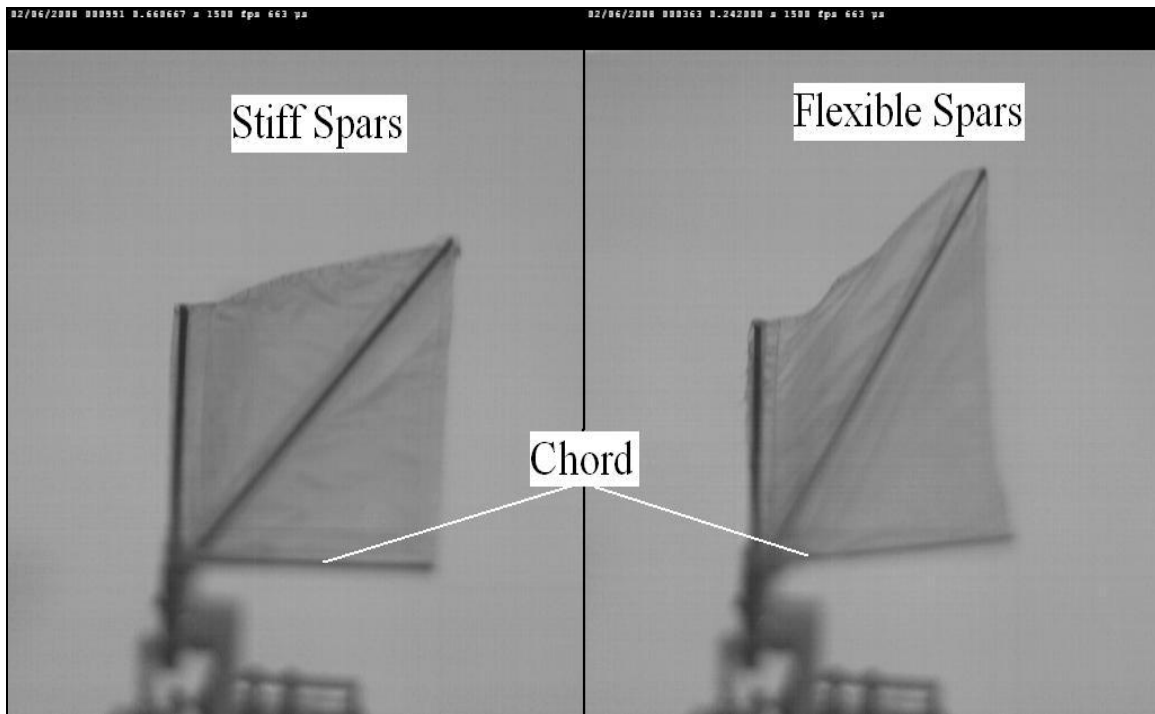
Figure 62: 4" x 2", 12.1" Span Wing Shape @ 4 Hz (Side Camera)
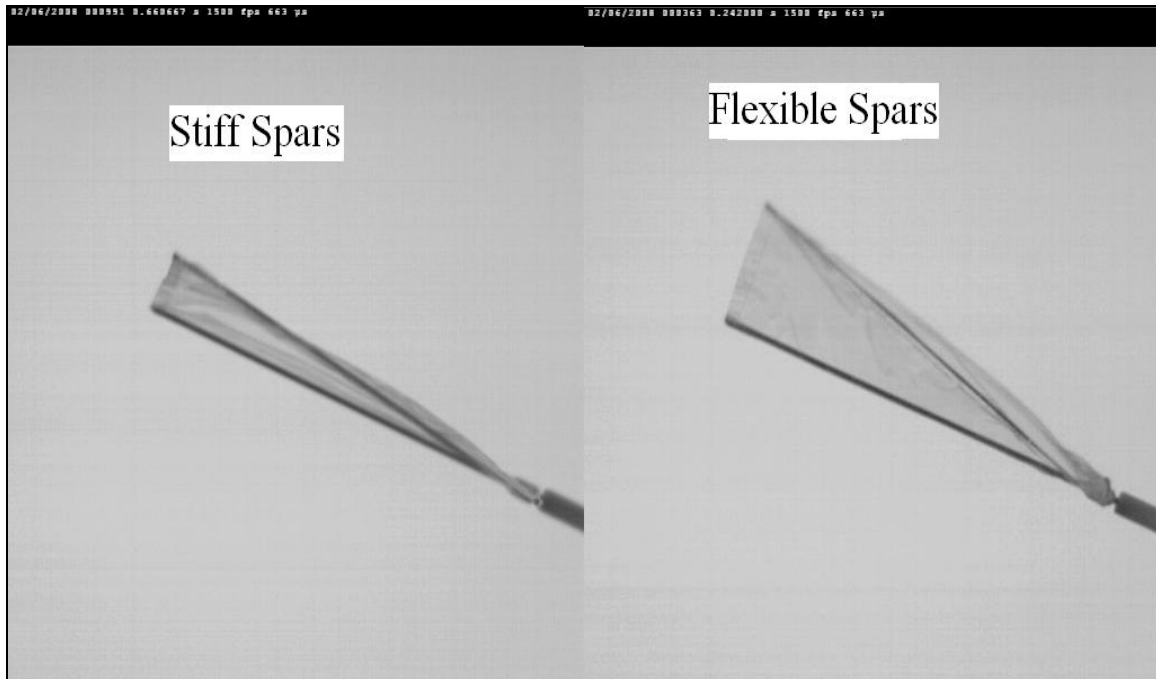
Figure 63: 4" x 2", 12.1" Span Wing Shape @ 4 Hz (Back Camera)

This set of pictures shows how the smaller diameter carbon fiber rods have an effect on the overall shape of the wing. The component which has the most influence on this shape is the piece that defines the chord, and is securely fixed to the leading edge spar. As this component bends inward toward the center of the wing, the spar that spans across the middle of the wing begins to lag further behind the leading edge. The resultant shape of the wing causes the higher thrust for the flexible wing at lower flapping frequencies. The second set of images were taken with a flapping frequency of 7.5 Hz, shown in Figure 64 and Figure 65.

Figure 64: 4" x 2", 12.1" Span Wing Shape @ 7.5 Hz (Side Camera)
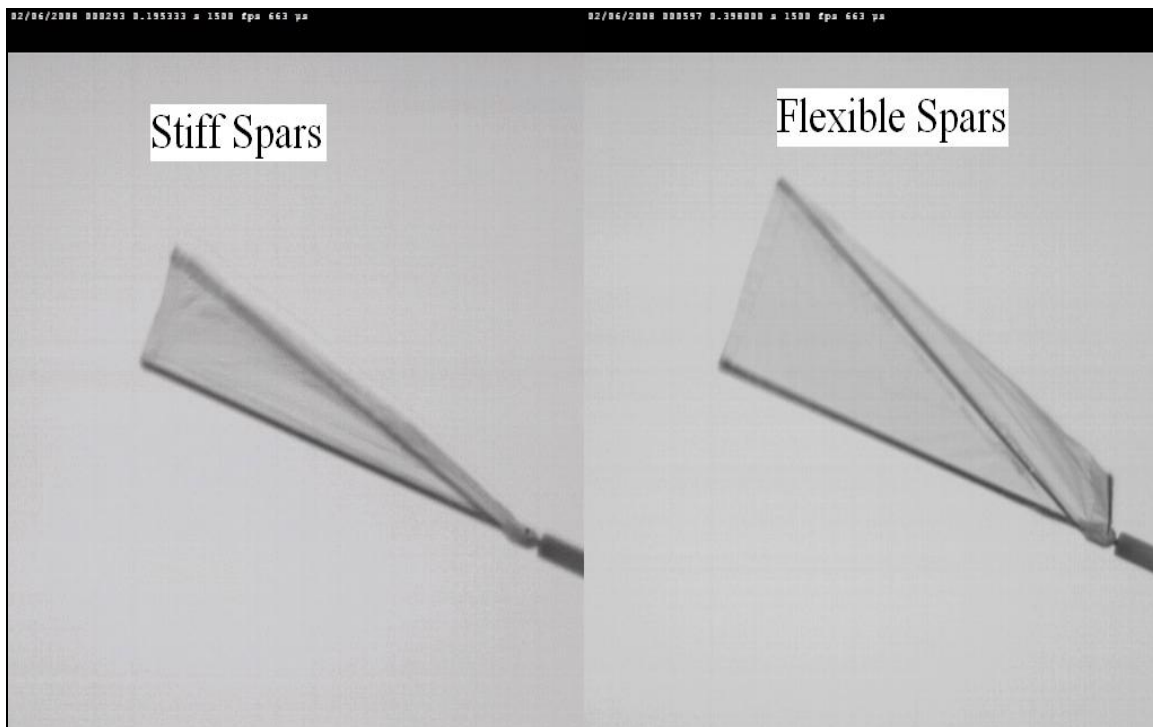
Figure 65: 4" x 2" , 12.1" Span Wing Shape @ 7.5 Hz (Back Camera)

77

At this higher flapping frequency, it is clear to see how the flexible wing has a much more deformed shape than at 4 Hz. This may account for why the thrust for flexible wing decreased at frequencies above 6.5 Hz when compared to the stiff wing. An example of a wing in motion can be seen in Figure 66, where individual frames were taken from the high speed video. This particular video is of the 4" x 2" flexible and stiff wings flapping at 7.5 Hz, as viewed from the rear and side cameras.

Frames	Flexible Wing		Stiff Wing	
	Rear Camera	Side Camera	Rear Camera	Side Camera
1				
15				
30				
45				
60				
75				
90				

Figure 66: High Speed Video Frame Analysis (Flexible vs. Stiff Wing)

4.4   Photogrammetry

A model was fabricated to simulate the contour of a flapping wing that can be used with the photogrammetry program Photomodeler. In order to determine if the high speed cameras would be compatible with the program, still images were taken of the model from four different angles. The camera was placed above the model looking down at a 45 degree angle, and the model was rotated clockwise approximately 90 degrees between images. Once the images were acquired, they were loaded into Photomodeler where the targets could be marked and automatically oriented by the program. A pair of images used for the target marking process can be seen in Figure 67.
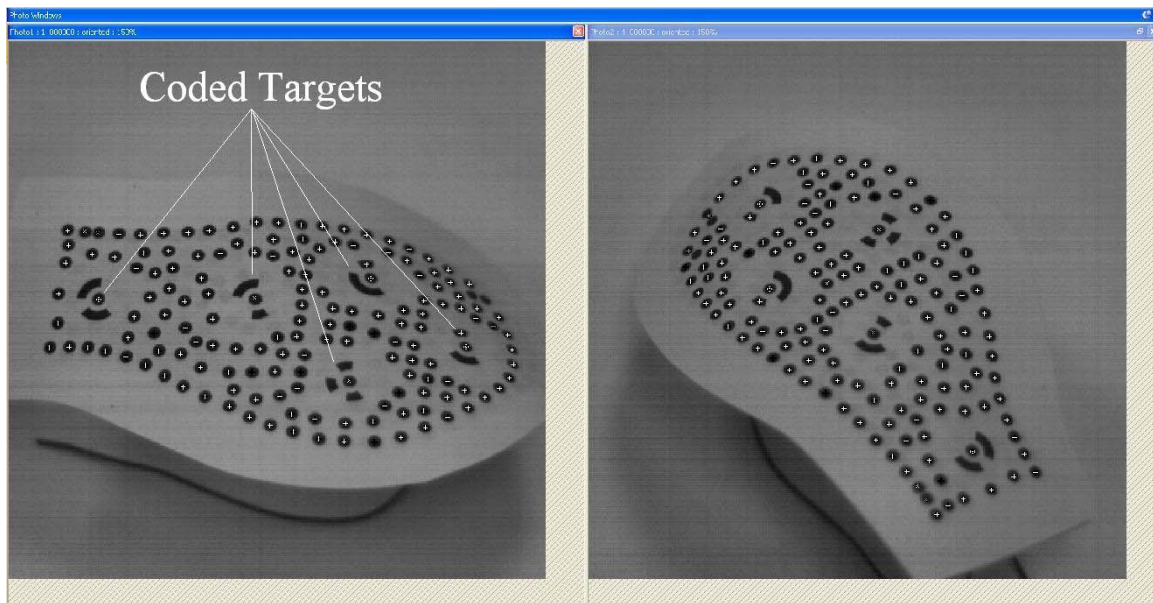
Figure 67: Test Images Marked Using Photomodeler

The five coded targets that resemble bulls-eyes with broken circles are automatically recognized by the program, which allows multiple pictures to be oriented

without any input from the user. Once the targets have been marked in all four images, a three-dimensional rendering of the model is created. This rendering can be seen in Figure 68. All of the white points which make up the 3-D rendering represent the targets placed on the model. This means the resolution of the 3-D rendering is dependent on the number of targets placed on the object of interest. The distance between any two points can also be calculated with the aid of a reference distance.
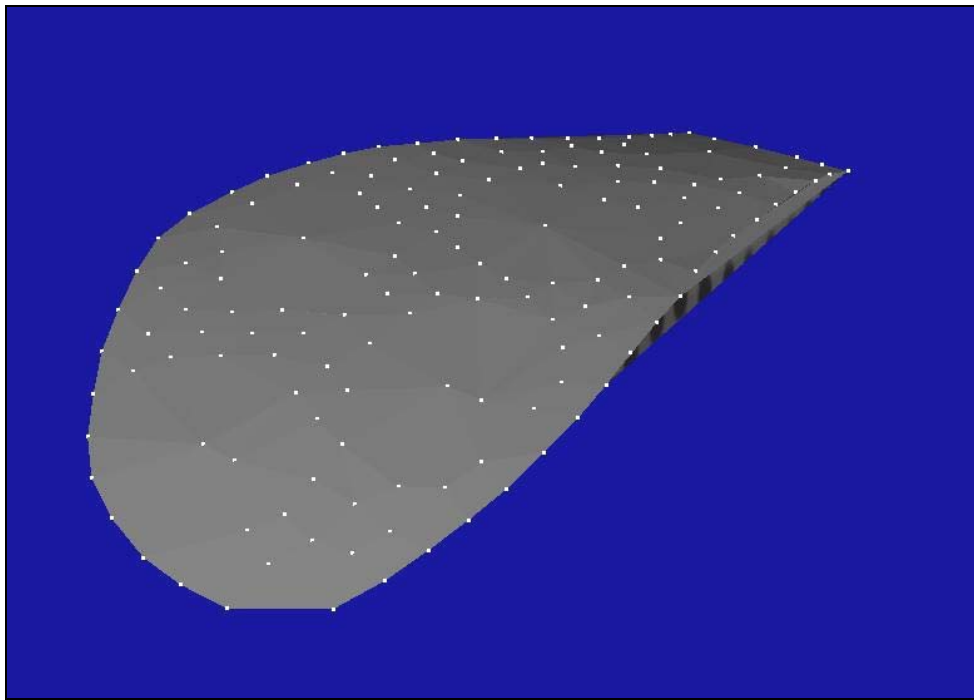
Figure 68: Photomodeler 3-Dimensional Wing Shape

Overall, even though this was a preliminary study of photogrammetry, similar techniques can be used to study the behavior of a wing in motion. Results from this type of analysis can potentially be used for validating computer models of flapping wing kinematics.

5. Conclusions

5.1   Results Summary and Conclusion

The goal of this research was to prove out various fabrication methods and measurement systems that can be used to test flapping-wing MAVs. Several fabrication and measurement tools were used including SolidWorks CAD software and an Objet three-dimensional printer for designing and fabricating flapping mechanisms, an air-bearing table with force transducers and six degree-of-freedom balance for loads measurements, and a high speed camera system for wing deformation analysis and preliminary photogrammetry studies.

The aluminum table supported by linear air bearings along with a 50-gram capacity load cell proved to be a viable test bed for small scale thrust measurements, with an accuracy of $\pm$ 0.1 gram. This system successfully allowed for static thrust measurements to measure a time averaged force. This particular setup can also be adapted to measure a force in any direction by changing the orientation of the flapping mechanism. The power supplied to the motor was measured, and for selected configurations the thrust number, motor-specific power number, and a figure of merit were determined.

The AFIT-2 Modern Machine and Tool six degree-of-freedom force balance was able to sense time-accurate data of the normal force for the flapping mechanism at flapping speeds up to 7.5 Hz. With the LabView virtual instrument capable of collecting

data at a rate of 1000 Hz, the flapping frequency mechanism can be increased and still have sufficient resolution for gathering time-accurate data.

Dual X-Stream XS-4 high speed cameras were proven to provide images compatible with the photogrammetry program Photomodeler from EOS Systems incorporated. Even though collecting real-time data of the wing in motion was not performed due to the limited number of cameras, the resolution of the camera was adequate for use with the Photomodeler software. The high speed cameras proved to be a useful tool for visualizing the behavior of the wing at full speed. Both of the cameras were also capable of being synchronized to capture video of the flapping mechanism from two separate angles simultaneously.

The study of spar stiffness and wing flexibility with the 4" x 2", 12.1" span wing configuration produced results consistent with previous research conducted by Ho at the University of California, Los Angeles and Wilson and Wereley at the University of Maryland. At slower flapping speeds (3.5-6.5 Hz), the more flexible wing configuration led to higher thrust per unit power.

The three proof-of-concept 3-D models were drawn in SolidWorks. The drawing suggests that a flapping stroke, an out-of-plane sweeping stroke and wing pitching rotation can be controlled with a single crankshaft. The flapping-only model designed in SolidWorks and fabricated using the Objet 3-D printer proved to be a viable mechanism for use throughout this research. The flapping-pitch mechanism with two degrees of freedom was successfully designed and tested in SolidWorks, and can be fabricated for use in researching the effects of actively changing the pitch of a flapping wing.

5.2   Desired Impact of this Research

The information provided in this paper should enable researchers to utilize a similar system for testing flapping wing micro air vehicles. With additional development, more complex flapping mechanisms can be designed and fabricated ultimately leading to a fully operational flapping wing MAV. This experimentation has set the foundation for further testing utilizing the equipment and methodology developed throughout this research.

5.3   Recommendations for Future Experimentation

In order to have a better understanding of the inertial forces associated with the flapping mechanism, repeating the tests in an evacuated environment would aid in isolating the inertial loads. This could be achieved by performing the tests with the force balance and model mounted inside in a vacuum chamber. Perhaps the best configuration would be to have a clear glass or acrylic chamber that can be easily removed while allowing easy visual access to the experiment. Visual access would be a key factor in studying the behavior of the wings with the high speed cameras.

Significant research can also be conducted in the area of photogrammetry, however, certain issues must be addressed in order for photogrammatic studies to be possible. First and foremost, a system with at least three high speed cameras is needed for performing any type photogrammetry. The system used for this research was a two camera system, which made it impossible for using it with photogrammetry on a model in

motion. The next issue with photogrammetry would be to find a feasible method for placing targets on the membrane of the wing. These targets must be visible to the cameras while being extremely light weight. The weight of the targets becomes important in order to have a minimal affect on the physical properties of the wings. If photogrammetry proves to be a viable method for measuring the physical parameters of a flapping wing in motion, computational models for wing behavior can be developed and compared real-world photogrammetry data.

Lastly, more complex flapping mechanisms capable of wider ranges of movement may be beneficial for studying the affects of variable wing pitch and the out-of-plane flapping motion used for hovering in nature. Possible mechanisms may contain different types of actuators and stronger, lighter materials. More research should also be conducted with different wing geometries and building materials to better understand wing behavior and performance characteristics.

Configuration #1
Wing = (4" x 2 ")
Span (in)
12.1
Density (g/cm^3)
1.2

RATE (Hz)	FORCE (grams)	#2	#3	#4	#5	#6	#7	#8	#9	#10	#11	#12
3.5	0.7	0.7	0.7	0.6	0.5	0.5	0.55	0.6	0.55	0.5	0.55	0.6
4	0.8	0.95	0.9	1	0.8	0.7	0.75	0.78	0.8	0.75	0.8	0.8
4.5	1.05	1.1	1.1	1.05	1	0.95	0.95	1.07	1.05	1.1	1.05	1.1
5	1.35	1.45	1.4	1.5	1.3	1.35	1.4	1.43	1.4	1.45	1.5	1.4
5.5	1.75	1.8	1.9	2	1.75	1.8	1.85	1.85	1.8	1.85	1.8	1.9
6	2.3	2.2	2.35	2.25	2.2	2.3	2.3	2.25	2.3	2.25	2.3	2.25
6.5	3	2.9	3.05	3	2.9	2.85	2.85	2.8	2.75	2.8	2.8	2.75
7	3.5	3.4	3.45	3.5	3.35	3.45	3.3	3.4	3.2	3.3	3.35	3.4
7.5	4.2	4.2	4.2	4.1	3.95	4.1	4.05	4	3.9	3.95	3.85	3.8

#13	#14	#15	#16	#17	#18	#19	#20	Avg Thrust (grams)		Thrust Coeff.	
0.55	0.5	0.5	0.55	0.55	0.57	0.6	0.55		0.571		1.81208E-06
0.7	0.8	0.75	0.7	0.73	0.75	0.8	0.75		0.7905		1.9207E-06
1.1	1.1	1.1	1.05	1.1	1.07	1.1	1.05		1.062		2.03881E-06
1.45	1.45	1.5	1.45	1.43	1.41	1.45	1.45		1.426		2.21747E-06
1.95	1.9	1.9	1.85	1.9	1.87	1.9	1.95		1.8635		2.39487E-06
2.35	2.3	2.35	2.3	2.3	2.35	2.3	2.31		2.2905		2.47346E-06
2.8	2.8	2.85	2.8	2.77	2.83	2.8	2.8		2.845		2.61778E-06
3.3	3.3	3.4	3.35	3.34	3.37	3.4	3.36		3.371		2.67448E-06
3.85	3.9	3.85	3.85	3.82	3.9	3.87	3.9		3.962		2.73823E-06

Avg Thrust (Newtons)		Thrust Coeff.		Amps	Volts	Watts
0.0055958		0.042361718		0.25	1.5	0.375
0.0077469		0.044900941		0.28	1.6	0.448
0.0104076		0.047662085		0.32	1.9	0.608
0.0139748		0.051838576		0.39	2.1	0.819
0.0182623		0.055985759		0.44	2.3	1.012
0.0224469		0.057823097		0.53	2.7	1.431
0.027881		0.061196856		0.58	3	1.74
0.0330358		0.062522484		0.68	3.3	2.244
0.0388276		0.064012604		0.74	3.5	2.59

Configuration #2

Wing = (3.5" x 1.75 ")
Span (in)
11.1
Density (g/cm^3)
1.2

RATE (Hz)	FORCE (grams)	#2	#3	#4	#5	#6	#7	#8	#9	#10	#11	#12
5	0.65	0.6	0.6	0.65	0.65	0.6	0.65	0.6	0.6	0.65	0.65	0.6
6	1.15	1.05	1.1	1.05	1.1	1.15	1.15	1.05	1.05	1.1	1.15	1.1
7	1.85	1.8	1.8	1.9	1.85	1.8	1.85	1.9	1.85	1.85	1.8	1.9
8	2.55	2.6	2.55	2.6	2.6	2.65	2.65	2.55	2.55	2.65	2.6	2.6
9	3.6	3.7	3.7	3.65	3.7	3.75	3.7	3.7	3.7	3.65	3.65	3.65

#13	#14	#15	#16	#17	#18	#19	#20	Avg Thrust (grams)		Thrust Coeff.	
0.65	0.65	0.6	0.6	0.6	0.65	0.6	0.6		0.6225		1.36687E-06
1.15	1.05	1.15	1.1	1.1	1.15	1.05	1.1		1.1025		1.68114E-06
1.85	1.85	1.8	1.9	1.85	1.85	1.8	1.85		1.845		2.06694E-06
2.55	2.65	2.6	2.55	2.55	2.6	2.55	2.6		2.59		2.2215E-06
3.6	3.6	3.7	3.65	3.7	3.65	3.65	3.6		3.665		2.4838E-06

Avg Thrust (Newtons)		Thrust Coeff.		Amps	Volts	Watts
0.0061005		0.031953796		0.28	1.7	0.476
0.0108045		0.039300603		0.36	2.1	0.756
0.018081		0.048319608		0.42	2.5	1.05
0.025382		0.05193294		0.55	3	1.65
0.035917		0.058064685		0.71	3.6	2.556

Configuration #3

Wing = (3" x 1.5")
Span (in)
10.1
Density (g/cm^3)
1.2

RATE (Hz)	FORCE (grams)	#2	#3	#4	#5	#6	#7	#8	#9	#10	#11	#12
7	0.7	0.67	0.64	0.69	0.66	0.63	0.67	0.65	0.62	0.65	0.68	0.65
8	1.05	1	1.08	1.05	1.07	1.08	1.08	1.05	1.05	1.05	1.07	1.1
9	1.6	1.65	1.69	1.6	1.58	1.59	1.55	1.6	1.55	1.6	1.6	1.6
10	2.3	2.25	2.32	2.3	2.27	2.31	2.35	2.3	2.25	2.32	2.3	2.3
11	3.2	3.05	3.15	3.2	3.2	3.2	3.2	3.1	3.15	3.17	3.2	3.1

#13	#14	#15	#16	#17	#18	#19	#20	Avg Thrust (grams)		Thrust Coeff.	
0.63	0.67	0.65	0.65	0.61	0.63	0.65	0.65		0.6525		1.06639E-06
1.05	1.08	1.03	1.05	1.06	1.05	1.05	1.08		1.059		1.3251E-06
1.55	1.57	1.57	1.55	1.6	1.58	1.55	1.6		1.589		1.57099E-06
2.3	2.25	2.3	2.28	2.29	2.25	2.27	2.3		2.2905		1.83427E-06
3.05	3.2	3.1	3.15	3.12	3.15	3.2	3.15		3.152		2.0861E-06

Avg Thrust (Newtons)		Thrust Coeff.		Amps	Volts	Watts
0.0063945		0.024929523		0.29	2.1	0.609
0.0103782		0.03097744		0.37	2.4	0.888
0.0155722		0.036725559		0.5	2.9	1.45
0.0224469		0.042880499		0.61	3.5	2.135
0.0308896		0.048767487		0.79	4.2	3.318

Configuration #4
Wing = (2.5" x 1.25")
Span (in)
9.1
Density (g/cm^3)
1.2

RATE (Hz)	FORCE (grams)	#2	#3	#4	#5	#6	#7	#8	#9	#10	#11	#12
8	0.63	0.64	0.59	0.65	0.63	0.6	0.65	0.63	0.6	0.65	0.61	0.6
9	0.8	0.85	0.8	0.82	0.85	0.85	0.85	0.8	0.79	0.85	0.83	0.84
10	1.1	1.09	1.05	1.05	1.1	1.05	1.1	1.1	1.05	1.1	1.03	1.07
11	1.4	1.4	1.4	1.45	1.4	1.4	1.4	1.45	1.45	1.4	1.4	1.45
12	1.7	1.7	1.65	1.7	1.65	1.65	1.7	1.7	1.65	1.68	1.69	1.68
13	2.05	2.1	1.95	2	1.98	2	1.99	2.05	2.05	2.05	2.1	2.1
14	2.45	2.6	2.5	2.55	2.45	2.5	2.5	2.45	2.49	2.45	2.5	2.5
15	2.9	3.2	2.85	2.9	2.95	2.95	2.85	2.9	2.9	2.85	2.89	2.9

#13	#14	#15	#16	#17	#18	#19	#20	Avg Thrust (grams)		Thrust Coeff.
0.58	0.63	0.65	0.61	0.65	0.63	0.6	0.65	0.624		1.18483E-06
0.85	0.8	0.8	0.83	0.84	0.85	0.8	0.85	0.8275		1.24147E-06
1.1	1.05	1.05	1.1	1.03	1.04	1.05	1.05	1.068		1.29785E-06
1.4	1.4	1.42	1.45	1.43	1.45	1.4	1.4	1.4175		1.42361E-06
1.7	1.7	1.65	1.7	1.68	1.7	1.65	1.65	1.679		1.41691E-06
2.05	2.08	2.09	2.05	2.1	2.1	2.05	2.1	2.052		1.47552E-06
2.43	2.46	2.5	2.45	2.45	2.43	2.46	2.6	2.486		1.54134E-06
3.1	3	3.05	3.05	3.1	2.95	2.98	3	2.9635		1.60057E-06

Avg Thrust (Newtons)		Thrust Coeff.		Amps	Volts	Watts
0.0061152		0.027698361		0.22	2.1	0.462
0.0081095		0.029022341		0.27	2.4	0.648
0.0104664		0.030340359		0.32	2.7	0.864
0.0138915		0.033280294		0.37	3	1.11
0.0164542		0.03312361		0.43	3.3	1.419
0.0201096		0.034493726		0.49	3.6	1.764
0.0243628		0.03603251		0.57	4	2.28
0.0290423		0.037417251		0.65	4.5	2.925

Configuration #5

Wing = (4" x 2")
(Flexible Ribs)
Span (in)
12
Density (g/cm^3)
1.2

RATE (Hz)	FORCE (grams)	#2	#3	#4	#5	#6	#7	#8	#9	#10	#11	#12
3.5	0.65	0.7	0.75	0.69	0.7	0.65	0.7	0.7	0.65	0.65	0.75	0.65
4	1	0.95	1	1	1.05	1.05	1.05	1	1	1.05	1	0.95
4.5	1.25	1.25	1.27	1.3	1.35	1.28	1.3	1.3	1.25	1.26	1.29	1.3
5	1.65	1.65	1.7	1.75	1.7	1.7	1.7	1.65	1.68	1.65	1.7	1.7
5.5	2.05	2.1	2.1	2.15	2.15	2.1	2.1	2.15	2.15	2.1	2.05	2.1
6	2.5	2.45	2.5	2.5	2.45	2.45	2.45	2.5	2.5	2.45	2.4	2.5
6.5	2.9	2.95	2.9	2.9	2.9	2.95	2.95	2.9	2.9	2.85	2.95	2.9
7	3.3	3.25	3.3	3.2	3.3	3.2	3.2	3.25	3.2	3.3	3.22	3.25
7.5	3.8	3.85	3.8	3.7	3.8	3.8	3.7	3.7	3.75	3.75	3.7	3.8

#13	#14	#15	#16	#17	#18	#19	#20	Avg Thrust (grams)		Thrust Coeff.	
0.75	0.7	0.7	0.65	0.7	0.68	0.7	0.7		0.691	2.26692E-06	
1	0.95	1.05	1.05	1	1	1.05	0.95		1.0075	2.53057E-06	
1.3	1.35	1.3	1.25	1.25	1.35	1.3	1.3		1.29	2.56011E-06	
1.75	1.65	1.65	1.7	1.65	1.7	1.7	1.75		1.689	2.71508E-06	
2.15	2.15	2.1	2.1	2.15	2.15	2.1	2.1		2.115	2.80982E-06	
2.5	2.45	2.45	2.5	2.5	2.48	2.5	2.5		2.4765	2.76458E-06	
2.95	2.95	2.9	2.9	2.9	2.85	2.9	2.95		2.9125	2.77034E-06	
3.2	3.2	3.25	3.2	3.25	3.2	3.25	3.2		3.236	2.65403E-06	
3.7	3.75	3.75	3.7	3.7	3.75	3.7	3.7		3.745	2.67561E-06	

Avg Thrust (Newtons)		Thrust Coeff.		Amps	Volts	Watts
0.0067718		0.052994647		0.31	1.8	0.558
0.0098735		0.059158223		0.32	1.9	0.608
0.012642		0.059848701		0.33	1.9	0.627
0.0165522		0.063471635		0.37	2	0.74
0.020727		0.065686336		0.39	2.2	0.858
0.0242697		0.064628768		0.44	2.3	1.012
0.0285425		0.064763344		0.47	2.7	1.269
0.0317128		0.062044384		0.52	2.8	1.456
0.036701		0.062548852		0.6	2.9	1.74

Appendix B: SolidWorks CAD Blueprints of Flapping Mechanism

Main Body

Crankshaft (half)

Ø0.09

Ø0.13

Ø0.25

0.30

0.25

Ø0.85

0.12

0.19

		DIMENSIONS ARE IN INCHES	NAME	DATE	
		TOLERANCES:			<COMPANY NAME>
		FRACTIONAL±	DRAWN		
		ANGULAR: MACH ± BEND ±	CHECKED		
		TWO PLACE DECIMAL ±	ENG APPR.		
		THREE PLACE DECIMAL ±	MFG APPR.		
		MATERIAL --	Q.A.		
			COMMENTS:		
NEXT ASSY	USED ON	FINISH --			
APPLICATION		DO NOT SCALE DRAWING			

SIZE A DWG. NO. REV.

SCALE:2:1 WEIGHT: SHEET 1 OF 1

Lower Support Arm

0.30

⌀0.31

0.73

0.10

0.20

0.20

1.15

		DIMENSIONS ARE IN INCHES		NAME	DATE			
		TOLERANCES:	DRAWN			<COMPANY NAME>		
		FRACTIONAL ±	CHECKED					
		ANGULAR: MACH ± BEND ±	ENG APPR.					
		TWO PLACE DECIMAL ±	MFG APPR.					
		THREE PLACE DECIMAL ±						
		MATERIAL	Q.A.					
		--	COMMENTS:					
NEXT ASSY	USED ON	FINISH				SIZE	DWG. NO.	REV.
		--				A		
APPLICATION		DO NOT SCALE DRAWING				SCALE:	WEIGHT:	SHEET 1 OF 1

Upper Support Arm

Ø0.30

0.10

0.30

Ø0.13

0.22

0.11

1.45

0.20

		DIMENSIONS ARE IN INCHES		NAME	DATE	<COMPANY NAME>		
		TOLERANCES:	DRAWN					
		FRACTIONAL ±	CHECKED					
		ANGULAR: MACH ± BEND ±	ENG APPR.					
		TWO PLACE DECIMAL ±	MFG APPR.					
		THREE PLACE DECIMAL ±						
			Q.A.					
		MATERIAL --	COMMENTS:					
NEXT ASSY	USED ON	FINISH --			SIZE A	DWG. NO.		REV.
APPLICATION		DO NOT SCALE DRAWING			SCALE 2:1	WEIGHT:	SHEET 1 OF 1	

93

Pivot Arm

1.75

0.25

0.20

0.30

∅0.08

∅0.06

∅0.20

0.16

		DIMENSIONS ARE IN INCHES TOLERANCES: FRACTIONAL ± ANGULAR: MACH ± BEND ± TWO PLACE DECIMAL ± THREE PLACE DECIMAL ±		NAME	DATE	<COMPANY NAME>		
			DRAWN					
			CHECKED					
			ENG APPR.					
		MATERIAL --	MFG APPR.					
			Q.A.					
			COMMENTS:					
NEXT ASSY	USED ON	FINISH --				SIZE A	DWG. NO.	REV.
APPLICATION		DO NOT SCALE DRAWING				SCALE 2:1	WEIGHT:	SHEET 1 OF 1

Motor Mount

0.50

0.07

0.20

0.11

0.83

0.29

0.60

DIMENSIONS ARE IN INCHES
TOLERANCES:
FRACTIONAL±
ANGULAR: MACH±   BEND ±
TWO PLACE DECIMAL   ±
THREE PLACE DECIMAL ±

MATERIAL
--

FINISH
--

DO NOT SCALE DRAWING

NEXT ASSY | USED ON

APPLICATION

NAME | DATE
DRAWN
CHECKED
ENG APPR.
MFG APPR.
Q.A.
COMMENTS:

<COMPANY NAME>

SIZE A | DWG. NO. | REV.

SCALE:2:1 | WEIGHT: | SHEET 1 OF 1

Force Balance Mount

Ø0.51

0.91

1.01

0.17

1.00

1.95

1.55

0.60

DIMENSIONS ARE IN INCHES
TOLERANCES:
FRACTIONAL ±
ANGULAR: MACH ± BEND ±
TWO PLACE DECIMAL ±
THREE PLACE DECIMAL ±

MATERIAL --

FINISH --

NEXT ASSY | USED ON
APPLICATION

DO NOT SCALE DRAWING

NAME | DATE
DRAWN
CHECKED
ENG APPR.
MFG APPR.
Q.A.
COMMENTS:

<COMPANY NAME>

SIZE A | DWG. NO. | REV.
SCALE 2:1 | WEIGHT: | SHEET 1 OF 1

Wing Brace

0.30

0.25

⌀0.03

⌀0.05

0.15

		DIMENSIONS ARE IN INCHES	NAME	DATE	<COMPANY NAME>		
		TOLERANCES:					
		FRACTIONAL±	DRAWN				
		ANGULAR: MACH± BEND ±	CHECKED				
		TWO PLACE DECIMAL ±	ENG APPR.				
		THREE PLACE DECIMAL ±	MFG APPR.				
		MATERIAL	Q.A.				
		--	COMMENTS:				
NEXT ASSY	USED ON	FINISH					
		--			SIZE DWG. NO.		REV.
APPLICATION		DO NOT SCALE DRAWING			A		
					SCALE:3:03 WEIGHT:	SHEET 1 OF 1	

97

Appendix C: LabView Filter and Scaling Factor Settings

	Normal Force	Axial Force
Filter Settings (Lowpass Cutoff Frequency)	20 Hz	10 Hz
Scaling Factor (Y = mX + b)	Slope (m) = 1838.24 Y Intercept (b) = -224.08	Slope (m) = -183.15 Y Intercept (b) = 98.72

Bibliography

Combes, S., Daniel, T., "Into Thin Air: Contributions of Aerodynamics and Inertial-Elastic Forces to Wing Bending in the Hawkmoth Manduca Sexta," *Journal of Experimental Biology*, Vol. 206, 18 May 2003, pp. 2999-3006.

Dudley, R., Ellington, C., "Mechanics of Forward Flight in Bumblebees. II. Quasi-Steady Lift and Power Requirements," *Journal of Experimental Biology*, Vol. 148, 1990, pp.53-88.

Ellington, C., "The Aerodynamics of Hovering Insect Flight", Philosophical Transactions of the Royal Society of London, Series B, Biological Sciences, Vol. 305, No. 1122, 1984, pp. 1-181.

Ellington, C., "The Novel Aerodynamics of Insect Flight: Applications to Micro-Air Vehicles," *Journal of Experimental Biology*, Vol. 202, 15 Sept. 1999, pp. 3439-3448.

Ennos, A., "The Importance of Torsion in the Design of Insect Wings," *Journal of Experimental Biology*, Vol. 140, 5 May 1988, pp. 137-160.

Eos Systems Incorporated (2007). PhotoModeler – Close Range Photogrammetry Software. < http://www.photomodeler.com/kb/1/> Retrieved: 27 Aug 07.

Gamble, BJ., "Experimental Analysis of Propeller Interactions with a Flexible Wing Micro-Air Vehicle," AFIT Thesis AFIT/GAE/ENY/06-M10 (March 2006)

Gautam, J., and Massey, K., "The Development of a Miniature Flexible Flapping Wing Mechanism for Use in a Robotic Air Vehicle," 45th AIAA Aerospace Sciences Meeting and Exhibit, Reno, Nevada. Jan. 2007.

Ho, S., Nassef, H., Pornsinsirirak, N., Tai, Y., Ho, C.M., "Unsteady Aerodynamics and Flow Control For Flapping Wing Flyers," *Progress in Aerospace Sciences*, Vol. 39, 2003, pp. 635-681.

Huber II, AF., "Death by a Thousand Cuts: Micro-Air Vehicles in the Service of Air Force Missions"' Occasional Paper No. 29, Air War College, Jul. 2002.

Isaac, K., Colozza, A., Rolwes, J., "Force Measurements on a Flapping and Pitching Wing at Low Reynolds Numbers," 44th AIAA Aerospace Sciences Meeting and Exhibit, Reno, Nevada. Sept. 2006.

McIntosh, S., Agrawal, S., Khan, Z., "Design of a Mechanism for Biaxial Rotation of a Wing for a Hovering Vehicle," IEEE/ASME Transactions of Mechatronics, Vol. 11, No. 2, Apr. 2006.

McMichael, J., and Francis, C., "Micro Air Vehicles - Toward a New Dimension of
Flight", Technical report, DARPA, 1997.

Noonan, K., Yeager, W., Singleton, J., Wilbur, M.,
Mirick, Paul H., "Wind Tunnel Evaluation of a Model Helicopter Main-Rotor
Blade With Slotted Airfoils at the Tip," NASA TP-211260, Dec. 2001.

Shyy, W., Jenkins, D., Smith, R., "Study of Adaptive Shape Airfoils at Low
Reynolds Number in Oscillatory Flow," AIAA, Vol. 35, , pp. 1545-1548, 1997.

Snyder, R. D., Beran, P.S., Parker, G. H., and Blair, M., "A Design Optimization Strategy
for Micro Air Vehicles", AIAA Paper 2007-1853, Presented at the 48th
AIAA/ASME/ASCE/AHS/ASC Structures, Structural Dynamics, and Materials
Conference, Honolulu, Hawaii, Apr. 23-26, 2007.

Stewart, K. and Albertani, R., "Experimental Elastic Deformation Characterization of a
Flapping-Wing MAV Using Visual Image Correlation," 3rd US-European
Competition and Workshop on Micro Air Vehicle Systems & European Micro Air
Vehicle Conference and Flight Competition, Toulouse, France, 17-21 Sept. 2007.

Wilson, N., and Wereley, N., "Experimental Investigation of Flapping
Wing Performance in Hover", AIAA Paper 2007-1761, Presented at the 48th
AIAA/ASME/ASCE/AHS/ASC Structures, Structural Dynamics, and Materials
Conference, Honolulu, Hawaii, Apr. 23-26, 2007.

Wootton, R., Herbert, R., Young, P., Evans, K., "Approaches to the Structural Modeling
of Insect Wings," *Philosophical Transactions of the Royal Society of London B:
Biological Sciences*, Vol. 358, No. 1437, 29 Sept. 2003, pp. 1577-1587.

1. REPORT DATE *(DD-MM-YYYY)* 27-03-2008	2. REPORT TYPE Master's Thesis	3. DATES COVERED *(From – To)* Sep 2007 – Mar 2008

4. TITLE AND SUBTITLE	5a. CONTRACT NUMBER
BIOMIMETIC MICRO AIR VEHICLE TESTING DEVELOPMENTAND SMALL SCALE FLAPPING-WING ANALYSIS	5b. GRANT NUMBER
	5c. PROGRAM ELEMENT NUMBER
6. AUTHOR(S) Svanberg, Craig E., Second Lieutenant, USAF	5d. PROJECT NUMBER
	5e. TASK NUMBER
	5f. WORK UNIT NUMBER

7. PERFORMING ORGANIZATION NAMES(S) AND ADDRESS(S) Air Force Institute of Technology Graduate School of Engineering and Management (AFIT/EN) 2950 Hobson Street, Building 642 WPAFB OH 45433-7765	8. PERFORMING ORGANIZATION REPORT NUMBER AFIT/GAE/ENY/08-M27

9. SPONSORING/MONITORING AGENCY NAME(S) AND ADDRESS(ES) AFRL/RBSB Attn: Parker, Gregory H. Maj 2210 Eighth St. WPAFB, OH 45433	10. SPONSOR/MONITOR'S ACRONYM(S)
	11. SPONSOR/MONITOR'S REPORT NUMBER(S)

12. DISTRIBUTION/AVAILABILITY STATEMENT
APPROVED FOR PUBLIC RELEASE; DISTRIBUTION UNLIMITED.

13. SUPPLEMENTARY NOTES

14. ABSTRACT

The purpose of this research was to develop testing methods capable of analyzing the performance of a miniature flapping-wing mechanism that can later be adapted for the development a biomimetic flapping-wing micro air vehicle (MAV). Three small scale flapping mechanisms capable of single plane flapping, flapping with active pitch control, and flapping/pitch with out-of-plane movement were designed using SolidWorks. The flapping-only model was fabricated on an Objet 3-dimensional printer and miscellaneous parts. The flapping mechanism was mounted on a supported by air bearings, and thrust was measured for a variety of conditions. The testing was conducted using wings composed of carbon fiber and Mylar in four different size configurations, with flapping speeds ranging from 3.5 – 15 Hertz. The thrust was measured using an axially mounted 50 gram load cell which resulted in an accuracy of $\pm$ 0.1 gram. The flapping mechanism was then mounted on a 6-component force balance to measure dynamic loading, which demonstrated the ability to gather time-accurate data within a single flapping stroke at speeds as high as 15 Hz. High speed cameras were also used for capturing images of how the structure of the wing changed at various testing conditions. Overall this research successfully demonstrated testing procedures that can be utilized in developing small scale flapping-wing micro air vehicles.

15. SUBJECT TERMS
Biomimetic MAV, Flapping-Wing MAV Testing, MAV, Micro Air Vehicle

16. SECURITY CLASSIFICATION OF:			17. LIMITATION OF ABSTRACT	18. NUMBER OF PAGES	19a. NAME OF RESPONSIBLE PERSON Dr. Mark F. Reeder
1. REPORT	2. ABSTRACT	c. THIS PAGE			19b. TELEPHONE NUMBER *(Include area code)*
U	U	U	UU	114	(937) 255-3636, x4530 e-mail: mark.reeder@afit.edu

Standard Form 298 (Rev. 8-98)
Prescribed by ANSI Std. Z39-18